This is a preprint, the final version is subject to change, of the American Mineralogist (MSA)
Cite as Authors (Year) Title. American Mineralogist, in press.
DOI: https://doi.org/10.2138/am-2018-6541

REVISION 2

Dehydrogenation and dehydroxylation as drivers of the thermal decomposition of Fe-chlorites

Małgorzata Lempart (1) *, Arkadiusz Derkowski (1) *, Katarzyna Luberda-Durnaś (1), Michał Skiba (2), Artur Błachowski (3)

(1) Institute of Geological Sciences, Research Centre in Krakow, Senacka St. No. 1, PL-31002 Krakow, (2) Institute of Geological Sciences, Jagiellonian University, Gronostajowa St. No. 3a, PL-30 387, Krakow (3) Institute of Physics, Pedagogical University, Podchorazych St. No. 2, PL-30 084 Krakow

* Corresponding authors. Email: ndlempart@cyf-kr.edu.pl (M. Lempart); ndderkow@cyf-kr.edu.pl (A. Derkowski)

Abstract

In addition to dehydroxylation, thermal decomposition of Fe(II)-bearing chlorites involves also dehydrogenation. Dehydrogenation does not require the presence of oxygen and readily occurs in an inert gas atmosphere via electron transfer between the OH group and octahedral Fe(II). The reaction results in releasing one hydrogen atom that forms H_2 gas upon diffusing out of the crystallite, and leaves one structural Fe(II) oxidized, to keep the charge balance. Dehydrogenation removes structural hydrogen reducing the amount of OH groups available for dehydroxylation thus H_2O released during heating.

In the present study the dehydrogenation was tracked thermogravimetrically (TG) for pure chlorites. Clinochlore, Fe-clinochlore, and Mg-chamosite were investigated under various isothermal and ramp-heating conditions under pure nitrogen flow. Thermally-altered

Mg-chamosite was analyzed ex-situ using Mössbauer spectroscopy, X-ray diffraction (XRD), and infrared spectroscopy.

Dehydrogenation and dehydroxylation were found to occur simultaneously (in time), but independently (in mechanism) during the heating of all Fe(II)-containing chlorites. The extent of these reactions was tracked using a combination of total mass loss and degree of Fe(II) oxidation. The dehydrogenation/dehydroxylation ratio varied with heating conditions. The slower the ramp heating rate, thus longer time at elevated temperatures before dehydroxylation starts, the greater the dehydrogenation that precedes dehydroxylation. Each studied chlorite had its unique range of isothermal temperatures where dehydrogenation can be enhanced with only minor dehydroxylation. For Mg-chamosite, a narrow range of isothermal temperatures, 390-410°C, caused – after 48h of heating – the oxidation of almost 70% of Fe(II), with respect to a maximum ~20% of oxidized Fe(II) after dehydroxylation-dominated ramp heating. Any lower or higher isothermal temperatures than the optimum resulted in a lower amount of Fe(III) and greater total mass losses. Enhanced dehydrogenation led to the formation of a discrete population of a ferric (oxy) chamosite phase, observed in XRD patterns with a d-space of 13.91 Å, coexisting with 14.17 Å of the original chamosite. The dehydroxylation and dehydrogenation of chamosite at 450°C resulted in the broadening of 00*l* XRD reflections interpreted as a mixed-layer phase that consisted of original, dehydroxylated, and dehydrogenated layers. Each particular heating protocol enhancing either dehydroxylation or dehydrogenation resulted in different compositions of the product formed after chlorite structure breakdown at 1000°C.

Even with ramp heating, dehydrogenation can occur, especially with Fe(II)-rich chlorites, decreasing the total mass loss. The procedure for the determination of "structural water" content and "loss on ignition" and "total mass loss" commonly measured in rocks and

minerals by thermogravimetric methods can be questioned for iron (II)-bearing chlorites and hence in the case of all iron (II)-containing phyllosilicates.

In geological conditions, if dehydrogenation occurs prior to chlorite dehydroxylation, the quantity of "structural water" transported within chlorites to the metamorphic environment in subduction zones can be reduced even by 50%. If occurring in natural conditions, Fe(II)-oxidizing dehydrogenation reaction questions the applicability of chlorite in geothermometry. Increased Fe(III)/total Fe ratio results in the miscalculation of chlorite formation temperature as much as by hundreds °C. The presence of Fe(III) as a result of dehydrogenation should be considered for all Fe(II)-bearing phyllosilicates.

Keywords: chlorite, dehydrogenation, dehydroxylation, oxidation, thermogravimetry, Mössbauer spectroscopy

Introduction

Chlorites occur abundantly in various environments, from low to intermediate-grade metamorphic mafic and ultramafic rocks, in soils and sediments, forming as diagenetic alteration products of ferromagnesian minerals (Deer et al. 1992). Among all common phyllosilicates, chlorites have one of the highest contents of the OH groups (up to ~13 wt% of "structural water" equivalent), which makes them key minerals in the investigation of transport and melting processes in subduction zones (Grove et al. 2012; Manthilake et al. 2016). Chlorites are widely used as a geothermometer, the Fe^{2+} to total Fe ratio is especially sensitive to formation temperature and redox conditions (Inoue et al. 2009; Bourdelle et al. 2013; Lanari et al. 2014; Vidal et al. 2016).

The structure of tri-,trioctahedral chlorite, which is the most common variety, contains two octahedral sheets: one is sandwiched between two tetrahedral sheets (2:1 layer) and the other occurs in the interlayer. In the latter sheet, three octahedral cations (e.g. Mg^{2+}, Fe^{2+}, Fe^{3+} and/or Al^{3+}) are coordinated by six hydroxyl groups, whereas in the 2:1 layer, three octahedral cations (e.g. Mg^{2+} and/or Fe^{2+}) are coordinated by four oxygen atoms and two hydroxyl groups. Like other phyllosilicates, upon heating, the chlorite structure undergoes dehydroxylation, which involves the formation and elimination of water molecules. The first model of dehydroxylation, common in dioctahedral 2:1 layer minerals, represents an interaction of neighboring OH groups forming a H_2O molecule that diffuses along the interlayer whereas the residual oxygen, O_r remains in the structure (Vedder and Wilkins 1969; Guggenheim et al. 1987; Drits et al. 1995, 2012a,b), as following:

$$(OH)_{2n} \rightarrow nH_2O + nO_r \quad (1a)$$

A dehydroxylation model that involves protons H^+ migration to a donor OH groups where H_2O is formed and released was postulated for trioctahedral 2:1 layer phyllosilicates (Wang et al. 2015 and references therein):

$H^+ + (OH)^- \rightarrow H_2O$ (1b)

In terms of mass loss, the proton migration model results in the same value as the Equation 1a (one H_2O molecule released from two OH groups).

Due to the bimodal distribution of OH groups in the chlorite structure, their dehydroxylation occurs in a broad range of temperatures, from 400 to 850°C, depending on the chemical composition, distribution of octahedral cations, polytypism, and crystallite thickness (cf. Post and Plummer 1972; Borggaard et al. 1982; Prieto et al. 1991; Zhan and Guggenheim 1995; Steudel et al. 2016). The release of H_2Oduring chlorite dehydroxylation should occur in two steps, with a ratio of approximately 3:1, corresponding to the number of hydroxyls involved in the following exemplary reactions:

$$[(R_2^{2+}R^{3+})_3(OH)_6][(Si_3Al)R_3^{2+}O_{10}(OH)_2] \rightarrow [(R_2^{2+}R^{3+})_3O_3][(Si_3Al)R_3^{2+}O_{10}(OH)_2]+3H_2O\uparrow$$

$$\rightarrow[(R_2^{2+}R^{3+})_3O_3][(Si_3Al)R_3^{2+}O_{11}]+H_2O\uparrow \quad (2)$$

where R^{2+} stands for Mg^{2+}, Fe^{2+}, Mn^{2+}, and Ni^{2+} and R^{3+} is Al^{3+}, Fe^{3+}, Cr^{3+} and (R^{4+}) Ti^{4+}.

The dehydroxylation of the 2:1 layer in tri-,trioctahedral chlorite occurs at a higher temperature than that of the interlayer sheet (Zhan and Guggenheim 1995; Steudel et al. 2016) and results in a phase transition, thus structural collapse, as a trioctahedral structure cannot form a dehydroxylated phase the way that a dioctahedral structure can (Wang et al. 2015; cf. Drits et al. 1995). The prior dehydroxylation of the interlayer does not lead to a breakdown of the chlorite structure; however, it does lead to the formation of a "modified chlorite structure" (Villiéras et al. 1994; Zhan and Guggenheim 1995; Guggenheim and Zhan 1999). Although the dehydroxylation reaction and the partially dehydroxylated chlorite were subject to some studies (Bai et al. 1993; Villiéras et al. 1993, 1994; Zhan and Guggenheim 1995; Guggenheim and Zhan 1999), the mechanism responsible for the observed pathway of thermal decomposition is poorly understood in terms of chlorites' Mg-Fe variability (cf. Post and

Plummer 1972; Goodman and Bain 1979; Borggaard et al. 1982; Prieto et al. 1991; Steudel et al. 2016).

The oxidation reaction (both thermally and chemically induced) of ferrous iron in micas and amphiboles under oxidizing or neutral conditions involves not only the loss of H_2O (as dehydroxylation), but also the loss of hydrogen accompanied by the oxidation of Fe^{2+} to maintain the layer charge balance (e.g. Hodgson et al. 1964; Vedder and Wilkins 1969; Farmer et al. 1971; Sanz et al. 1983; Rancourt et al. 2001). In dehydrogenation, one hydrogen atom is released for each oxidized Fe^{2+} atom, due to an electron transfer:

$$Fe^{2+} + OH^- \rightarrow Fe^{3+} + O_r^{2-} + H^\bullet \uparrow \quad (3)$$

where $2H^\bullet$ radicals form H_2.

Because the dehydrogenation of OH groups coordinated to Fe^{2+} releases hydrogen, the number of OH groups available for dehydroxylation is decreased (Rouxhet et al. 1972; Rancourt et al. 2001; Steudel et al. 2016).

The dehydrogenation does not lead to the breakdown of the layer structure as dehydroxylation does (Rouxhet et al. 1972; Borggaard et al. 1982). Oxidative dehydrogenation can occur in an oxidizing gas atmosphere as well as in inert gas or vacuum conditions, without an incorporation of an external oxygen into the structure (Rouxhet et al. 1972; MacKenzie and Berezowski 1981; Sanz et al. 1983). But in an oxidizing gas atmosphere, $H^\bullet$ preferably reacts with any available oxygen to produce H_2O at the sample's surface:

$$4(Fe^{2+} + OH^-) + O_2 \rightarrow 4(Fe^{3+} + O_r^{2-}) + 2H_2O \quad (4)$$

(MacKenzie and Berezowski 1981).

In the case of chlorite, the additional hydroxyl groups and the presence of two Fe(II)-bearing octahedral sheets make the structure the most prone to dehydrogenation among all Fe(II)-containing phyllosilicates. Specific heating conditions may lead to the oxidation of all octahedral Fe^{2+} by dehydrogenation, especially in the case of chamosite (Brindley and Youell

1952; Goodman and Bain 1979; Borggaard et al. 1982; Steudel et al. 2016). However, other researchers assert that H_2O derived from dehydroxylation is needed for dehydrogenation (Villiéras et al. 1992). There exists a broadly accepted view that a dehydroxylation reaction alone can oxidize structural Fe^{2+} in chlorites and other phyllosilicates (Heller-Kallai and Rozenson 1980; Scott and Amonette 1985; Villiéras et al. 1992) as well as another view that dehydroxylation induces dehydrogenation (MacKenzie and Berezowski 1981; MacKenzie et al. 1986; Heller-Kallai et al. 1989).

Dehydrogenation is assumed to produce H_2 gas from H atoms released according to Equation 3 (Rouxhet et al. 1972; MacKenzie et al. 1986; Villiéras et al. 1992). Indeed, Villiéras et al. (1992) found H_2 liberated from chlorite, which was recently confirmed by Steudel et al. (2016) during ramp-heating of chamosite under a nitrogen gas atmosphere. Steudel et al. (2016) found that the H_2 release in chamosite was accompanied by the oxidation of 30% of Fe^{2+}. The Fe(II)-oxidizing dehydrogenation was observed also in Fe-clinochlores (Goodman and Bain 1979; Borggaard et al. 1982). Ramp heating enhances the dehydroxylation reaction, whereas long-term isothermal heating conditions were found to be the most favorable for dehydrogenation (Rouxhet et al. 1972; Hogg and Meads 1975; Rancourt et al. 2001). Therefore, in order to study the oxidation of Mg-chamosite by dehydrogenation Borggaard et al. (1982) applied only the prolonged thermal treatment. However, following Steudel et al. (2016) and Goodman and Bain (1979), the occurrence of dehydrogenation under ramp heating conditions cannot be ruled out in the case of Mg-Fe chlorites. On the other hand, Borggaard et al. (1982) did not observe dehydrogenation under inert gas conditions.

Although micas are simpler structures than chlorites and may serve as a model for dehydrogenation and dehydroxylation in chlorite's 2:1 layer, there is no agreement as to how both reactions proceed and how they are interrelated in these minerals. The interlayer

161 octahedral sheet adds complexity to the problem. In the present paper, the quantitative
162 assessment and interrelations between dehydroxylation and dehydrogenation are studied
163 whether they proceed separately and independently of one another following Equations 2 and
164 3, respectively. In addition, we have attempted to find the most favorable conditions where
165 one of the reactions prevails. The overall goal of our work was to explain considerable
166 variations in the interpretation of chlorite thermal decomposition and mass loss.
167

Samples characterization

Seven different tri-, trioctahedral chlorites representing a common Mg-Fe-series were studied in preliminary thermogravimetric experiments. In order to compare their thermal behavior, three representative samples differing in iron content and the distribution of Mg^{2+}, Fe^{2+}, Fe^{3+} and Al^{3+} between the sheets were selected for study (nomenclature from Bayliss 1975): clinochlore (CCC) from Flagstaff Hill, El Dorado County (CA, USA), Fe-clinochlore (Sptb) form Spitsbergen (Norway), Mg-chamosite (MtBl) from Plan de l'Aguille, Massif du Mont-Blanc (France). MtBl and Sptb samples were gently ground in an agate mortar to pass through a <0.1 mm sieve, to ensure the sample homogeneity. These samples consisted of plate-like gains with a size range 10-100μm and 50-100 μm, for MtBl and Sptb, respectively. CCC sample was ground with hexane in a McCrone mill ((MAC Accessories & Components,USA) for five minutes, what provided the particles of 2-100 μm, as determined with electron microscopy. Representative, homogeneous portions of the material were used in different experiments.

Bulk chemical composition was obtained via JEOL JXA-8230 electron microprobe analysis (EMPA) on sample grains embedded in epoxy resin and polished to the half of their thickness, to obtain a statistically valid analysis from randomly oriented crystallites. Individual crystals of chlorite were analyzed in wavelength-dispersion mode with an accelerating voltage of 15 kV, a probe current of 15 nA, and a beam diameter of 3-5μm. Counting time was 20s for peak and 20s for background in lower and upper position. The following standards, analytical lines and monochromators (TAP - thallium acid phthalate, PET – pentaerythritol, LIF - lithium fluoride) were used: Na, Al and Si (albite, Kα, TAP), Mg (diopside, Kα, TAP), Ti (rutile, Kα, PET), Cr (synthetic Cr_2O_3, Kα, LIF), Mn (rhodonite, Kα, LIF), Fe (fayalite, Kα, LIF), Ni (synthetic NiO, Kα, LIF) and Zn (willemite, Kα, LIF). No

192 zonation of chemical composition or heterogeneity was observed in high-contrast, back
193 scattered electron (BSE) images.

194 Based on powder X-ray diffraction (XRD), samples were classified as tri-,
195 trioctahedral II*b* chlorites with a monoclinic-shaped cell, with total impurities (mainly quartz)
196 content below 3%. Mössbauer spectroscopy was used to determine the Fe^{2+}/Fe^{3+} ratio. In
197 order to establish the distribution of total iron between the interlayer and 2:1 layer sheets,
198 refinements of XRD patterns were performed using Sybilla 2D software (proprietary Chevron
199 ETC); total Fe content and the number of vacancies were fixed according to the formula
200 obtained from chemical composition (Tab. 1); all the other parameters were optimized during
201 the refinement. The ratios of octahedral total iron occurring in the interlayer to 2:1 layer were
202 determined: 44:56, 48:52, and 54:46, for MtBl, Sptb, and CCC, respectively. Subsequently,
203 all cations were distributed using the assumption that trivalent octahedral cations (Fe^{3+}, Al^{3+},
204 Ni^{3+}, and Cr^{3+}) are located in the interlayer sheet, creating a net positive charge to balance the
205 net negative charge from the 2:1 layer (Foster 1962). Mn^{2+} was assumed to occur in the
206 interlayer whereas the octahedral vacancies were likely located in the 2:1 layer (Vidal et al.
207 2001). However, it is not possible to assert that the obtained number of vacancies is only an
208 artifact calculated from EMPA. Theoretical mass loss upon complete dehydroxylation,
209 $H_2O(+)$, was calculated based on chemical formulas, and the reaction corresponding to
210 Equation 1 (a.p.f.u.). Chemical compositions of all chlorites were given in Table 1. Structural
211 formulas per formula unit were calculated based on 14 oxygen atoms as follows:

212 MtBl – $[Fe^{2+}_{1.40}Mn_{0.08}Al_{1.33}Fe^{3+}_{0.19}(OH)_6][(Si_{2.65}Al_{1.35})\ (Fe^{2+}_{1.98}Mg_{0.92}\square_{0.1}\ )\ O_{10}(OH)_2]$; $H_2O(+)$
213 10.77 wt%;

214 Sptb– $[Fe^{2+}_{0.55}Mg_{1.175}Mn_{0.01}Al_{1.18}Fe^{3+}_{0.085}(OH)_6][(Si_{2.78}Al_{1.22})(Fe^{2+}_{0.78}Mg_{2.175}\square_{0.045})O_{10}(OH)_2]$;
215 $H_2O(+)$ 12.00 wt%;

CCC – $[Fe^{2+}_{0.16}Mg_{1.65}Mn_{0.01}Al_{1.04}Fe^{3+}_{0.115}Ni_{0.01}Cr_{0.01}(OH)_6][(Si_{2.85}Al_{1.15})(Mg_{2.7}Fe^{2+}_{0.274}\square_{0.025})O_{10}(OH)_2]$; H_2O(+) 12.56 wt%.

Experiments and analytical methods

Thermogravimetry

Thermogravimetric (TG) analysis was performed using a TA Discovery instrument (TA Instruments, USA), which had a weighing error of <1 μg, weight measurement accuracy of <0.1 μg, and a thermal drift between 200 and 1000°C of <4 μg. A 20 mg air-dried chlorite sample placed in a Pt crucible was heated in a dry nitrogen atmosphere (>99.999% purity) and with a flow rate of 100 cm^3 min^{-1}. For selected experiments a flow of dry synthetic air (>99.99% purity) was used with a rate 100 cm^3 min^{-1} instead of N_2. In another set of experiments, upon reaching 1000°C, the purging gas was changed to synthetic air and the sample was heated isothermally for 15 minutes in order to create oxidation conditions. Prior to any particular TG experiment, each sample was dried *in-situ* in the TG furnace isothermally for 10 min at 200°C to remove adsorbed water. Two types of TG experiments were performed: (1) ramp heating to 1000°C using different rates (5, 10, or 20°C min^{-1}), (2) isothermal heating with different temperatures and time intervals (selected between 350 and 625°C for 1-48 hours) followed by ramp heating to 1000°C at a rate of 10°C min^{-1}. An isothermal heating procedure was employed in the present study – each segment of the procedure is shown in Table 1 and Figure 1. In order to remove residual oxygen from the TG furnace, before each experiment the furnace and balance were purged with nitrogen gas at 10 cm^3 min^{-1} for 24 h followed by a purge using 100-200 cm^3 min^{-1} rate just before starting the experiment. To ensure an oxygen-free environment, CuC_2O_4 was analyzed periodically in the furnace purged under the above-mentioned conditions (standard reference material - TA Instruments). Selected TG experiments were repeated two times to check the reproducibility

of the results; a mean relative standard deviation of 0.15% was found for mass loss for isothermal heating alone (at 400°C for 48h) and 0.3% for ramp heating (10°C min^{-1} to 1000°C).

The calculation of mass loss for individual segments of TG experiments was based on the same points in each case (Fig. 1). The initial mass reference point (m_0) was placed at the end of isothermal drying at 200°C; Δm_{iso} denotes mass loss during the isothermal heating segment, whereas Δm_{ramp} represents mass loss for the ramp heating segment calculated as the difference between the mass at the end of the isothermal step and minimum mass recorded near 1000°C (m_{min} point). If switching to air were included at 1000°C, the end-point of the heating step under air corresponds to the last point of measurement (m_{air}). The total mass loss during the cited TG experiment, Δm_{dx}, is the difference between m_0 and m_{min} (Fig. 1). Material for ex-situ analysis was collected at the end of the isothermal segment (point m_{ramp} in Fig. 1), in selected experiments using a MtBl sample, and analyzed using Mössbauer spectroscopy, infrared (IR) spectroscopy, and XRD. The samples were labeled [Isothermal Temperature(°C)_Isothermal Time(h)] (e.g. 400_24). Two samples obtained after ramp heating to 1000°C at a rate of 10°C min^{-1} (point m_{min} on Fig. 1) were also collected – one from the experiment that did not involve any prior isothermal heating (sample labeled 10°C/min_N2 and 20°C/min_N2) and another one that had prior been subjected to an isothermal segment at 390°C for 48h followed by ramp heating to 1000°C (DX_390_48).

Mössbauer spectroscopy

Mössbauer transmission measurements were performed using a MsAa-3 spectrometer (RENON, Kraków, Poland) (Górnicki et al. 2007) equipped with an LND Kr-filled proportional detector and He-Ne laser-based interferometer. A single line commercial ^{57}Co(Rh) source kept at room temperature was applied for a 14.41-keV resonant transition in ^{57}Fe. The Mössbauer absorbers were prepared in powder form by mixing ~20 mg of the

investigated material with a B_4C carrier and lightly pressing in a sample holder between Mylar® window sheets aluminized on both sides. Hence, the absorber thickness equaled about 10 mg cm^{-2} of investigated material, as the circular sample holder has a 16 mm diameter. Spectra were collected for absorbers kept at room temperature and additionally at 80 K for the DX_390_48 sample. The measuring time was about 24 hours for each spectrum collected. Spectra were fitted using transmission integral approximation by means of a Mosgraf-2009 software suite. Spectral shifts were reported versus natural α-Fe at room temperature. Errors for all values are of the order of unity for the last digit shown or as stated.

X-ray diffraction

A Bruker D8 advanced diffractometer (Bruker, Karlsruhe, Germany) working using a Debye-Scherrer geometry with a CoKα X-ray tube (35kV, 40mA) was used in the study. The primary X-ray beam was monochromatized and formed using a Göbel mirror, 0.2 mm fixed divergence slit, 2.5˚ Soller slits, and a beam knife. A VANTEC detector with radial Soller and 2.5˚ Soller slits was used for the secondary beam. The scan range was set to 5 to 110°2θ with a step size of 0.014°2θ. To investigate structural changes in chlorites after TG heating, ex-situ capillary XRD measurements were performed using a 0.3 mm sodium glass capillary. The exact values of c* were fitted assuming a SPVII-split pseudo-Voigt peak-shape function in TOPAS software (version 5). Qualitative analysis was performed using EVA software (version 4.2.0.31) and the Crystallographic Open Database (COD) (Grazulis et al. 2009).

Infrared spectroscopy

Infrared (IR) spectra were recorded using a Nicolet 6700 spectrometer with DTGS KBr detector (Thermo Scientific, Waltham, Massachusetts, USA). *Ex-situ* analyses of heated samples were collected in transmission mode as 64-scan averages with 4 cm^{-1} resolution on a sample prepared in the form of KBr pellets (0.5 wt% of sample mixed with KBr). To obtain *in-situ* analyses of heated chlorites, spectra were collected using a Praying Mantis (by

Harrick, USA) diffuse reflection (DRIFT) accessory equipped with a high temperature reaction chamber. Each sample was mixed and ground with diamond powder (15% concentration). Spectra were measured at a resolution of 4 cm^{-1} with 256-scan averages in the range from 25 to 800°C. Before measurement, samples were kept at a selected temperature for 30 minutes under a dry nitrogen atmosphere (>99.999% purity) with a 400 cm^3 min^{-1} rate of flow.

Results

Thermogravimetry

Non-isothermal experiments. TG patterns of the studied tri-, trioctahedral chlorites revealed two major mass loss steps occurring in the temperature interval from 350°C to 850°C (Fig. 2). Total mass losses, Δm_{dx}, under a 10°C min^{-1} rate to 1000°C corresponding to complete dehydroxylation resulted in the following: 10.10 wt%, 11.50 wt%, and 12.45 wt%, for MtBl (Mg-chamosite), Sptb (Fe-clinochlore), and CCC (clinochlore), respectively; whereas the temperatures of the first major thermal effect were as follows: 550°C, 600°C, and 555°C, respectively. Mass evolution occurred in two steps, ~ 200°C apart, generally following the reaction (Eq.2), but did not match the theoretical 3:1 ratio associated with the number of hydroxyls belonging to the two hydroxide octahedral sheets. The boundary between these two thermal effects on DTG pattern was ambiguous. Because the studied chlorites are free from impurities that may increase or decrease mass loss, and the total theoretical mass loss due to dehydroxylation is nine times greater than potential mass loss due to dehydrogenation (compare Eqs. 2 and 3), the observed mass loss can tentatively be assigned as resulting from dehydroxylation. If dehydroxylation is the sole reaction during heating, according to Equation 2, experimental mass losses obtained under different heating conditions should match theoretical mass loss upon dehydroxylation calculated from the mineral formula. Indeed, in a

316 series of seven tri-, trioctahedral chlorites featuring varying Fe(II) content, the maximum
317 mass loss Δm_{dx} observed after TG ramp heating in an N_2 atmosphere with the highest rate of
318 20°C min^{-1} was closest to theoretical $H_2O(+)$ (Fig. 3, Tab. 2). The lower the Fe(II) content in
319 chlorite, the closer the Δm_{dx} obtained using different heating rates (Tab. 2). For Fe(II)-rich
320 chlorites, especially for MtBl, a tendency was observed whereby Δm_{dx} would decrease with a
321 decreasing rate of heating. The lowest Δm_{dx} was recorded in TG runs under synthetic air flow,
322 declining to nearly 50% of their $H_2O(+)$ values.

323 The DTG patterns of the MtBl sample ramp heated under nitrogen and synthetic air
324 gas atmosphere at 10°C min^{-1} rates to 1000°C are given in Figure 4a. The two-stage type of
325 DTG pattern under nitrogen gas changed to a single, uniform DTG event under synthetic air.
326 Under air, the maximum of the first DTG peak shifted downward ~50°C and the second
327 minor peak at ~700°C disappeared completely.

328 **Isothermal experiments.** To track the variations of mass loss observed with different heating
329 rates, a pure, Fe(II)-rich chlorite MtBl sample (3.38 a.p.f.u. of Fe(II)) was selected as the
330 primary material for isothermal experiments. Isothermal heating temperatures were selected
331 based on TG patterns from ramp heating experiments (Fig. 2) designed to occur prior to
332 dehydroxylation (cf. Borggaard et al. 1982). The same approach was applied to clinochlore
333 (CCC) and Fe-clinochlore (Sptb) in order to test for Δm_{dx} variability with respect to Fe(II)
334 content (1.33 a.p.f.u. and 0.43 a.p.f.u., respectively) and the distribution of cations between
335 octahedral sheets (Tab. 2).

336 Extending the isothermal time or increasing isothermal temperature resulted always in
337 an increase in Δm_{iso}. Total mass loss, Δm_{dx}, however, changed as well, following a different
338 TG pattern. Except for runs of 1h at 350 and 400°C, where no significant differences from the
339 10°C/min_N2 and 20°C/min_N2 samples (ramp heating only) occurred, every experiment
340 that involved an isothermal step resulted in a lower Δm_{dx} (Fig. 4a). With increasing

isothermal heating time, Δm_{dx} generally decreased, but the relationship with isothermal temperature was more complex. For a particular isothermal heating time (24 or 48 hours), a significant decline in Δm_{dx} was observed for TG runs with isothermal heating at 400°C; a 48h isothermal reduced Δm_{dx} to 7.8 wt% (Fig. 4a). Similarly, the most reduced Δm_{dx} values were obtained after heating for 48 h at two "neighboring" temperatures: 390 and 410°C. Any slightly lower (≤ 375°C) or higher (≥ 425°C) isothermal temperature resulted in higher Δm_{dx}. Isothermal heating at 450°C produced a Δm_{dx} closer to the Δm_{dx} obtained after isothermal heating at 350°C (Tab. 2). In selected experiments, where a 15-minute isothermal step at 1000°C under synthetic air was added after ramp heating, mass gain occurred resulting in the final mass loss point always at 6.4 wt% (Fig. 4a). The final mass obtained following additional oxidation corresponded to the total mass loss recorded for "10°C/min_AIR" ramp heating under synthetic air (Tab. 2), implying that the same, maximum extent of oxidation was reached under oxidation conditions, regardless of the heating pattern.

For both clinochlore samples, Sptb and CCC, the total mass losses (Δm_{dx}) were closer to $H_2O(+)$ values. The lowest Δm_{dx} was found for experiments involving 48 hours of isothermal heating, but with different isothermal temperatures ranges. A Δm_{dx} 1.0 wt% lower than the maximum Δm_{dx} recorded during ramp heating (sample 10°C-, 20°C/min_N2) was found for Sptb heated isothermally at 550°C, and subsequent heating at 600°C and 625°C gave the same differences. Whereas the Δm_{dx} of 0.7 wt% lower than the maximum occurred for CCC heated above 500°C.

The DTG curve of MtBl (Fig. 4b) consisted of two distinct thermal events – a first, large peak at 550°C and a second, lower peak at 720°C, accompanied by a minor peak at 660°C. The first peak generally shifted to lower temperatures with increasing time and isothermal heating temperature (Figs. 4c, d, e). After isothermal heating at 350°C for 24 or 48 hours, a new peak appeared near 490°C, adjacent to the low-temperature slope of the large

peak, whereas the intensity of the minor peak at 660°C decreased (Fig. 4c). Furthermore, after heating at 400°C for 24 hours, the second DTG peak at 720°C tentatively associated with OH in the 2:1 layer decreased significantly and completely disappeared after isothermal heating for 48 hours in the range 390-410°C (Fig. 4d). The latter high-temperature DTG peak, however, was present again after isothermal heating at 425°C, 450°C, and 475°C (Fig. 4e).

Infrared spectroscopy

The OH stretching region of the IR spectrum of MtBl before heating revealed a typical IR pattern of an Fe-rich tri-, trioctahedral chlorite (Figs. 5a, b) (cf. Shirozu 1985). The bands in the range 3700 – 3625 cm^{-1} came from OH stretching in the 2:1 layer (Shirozu 1985; Bishop et al. 2008). Considering the sample's octahedral cation composition, the bands at 3645 cm^{-1} and 3625 cm^{-1} likely originated from the $2Fe^{2+}Mg$–OH and $3Fe^{2+}$–OH arrangements, respectively (Hayashi and Oinuma, 1967; Rouxhet et al., 1972). Two broad bands near 3545 cm^{-1} and 3400 cm^{-1} correspond to the interlayer OH, ascribed to (SiSi)O–OH and (SiAl)O–OH stretching, respectively (Hayashi and Oinuma 1967; Shirozu 1980).

The series of MtBl spectra obtained following different isothermal heating experiments showed a strong, gradual reduction in band intensity in the OH-stretching region (Fig. 5a). The OH-stretching bands of both the 2:1 layer and the interlayer became reduced simultaneously until treated isothermally at 450°C for 24 hours, but to a different degree for each band. The same relative OH-band proportions as for non-heated MtBl were observed only for the 350_24 sample; any subsequent samples showed more substantially reduced OH-stretching bands from the interlayer sheet with respect to the 2:1 layer. In sample 350_24, a band at 3625 cm^{-1} attributed to $3Fe^{2+}$–$OH_{2:1}$ became smoother. The spectrum of sample 400_48 did not follow the observed trend of continuous and simultaneous intensity drop of both (i.e. 2:1 and interlayer) OH bands. In the sample the intensities of 2:1 related OH bands were strongly reduced and almost equal to that obtained for the 450_48 sample, while the

intensities of bands associated with interlayer OH were almost equal to thaose obtained for the 450_24 sample (Fig. 5a). The spectrum of the 450_48 sample was most affected by isothermal heating; OH-stretching interlayer bands virtually disappeared and only a broad band with a maximum close to 3585 cm^{-1} tentatively associated with $2MgFe^{2+}$–OH in the 2:1 layer persisted.

The DRIFT spectra of MtBl heated *in-situ* in the range of 200 – 800°C reflected the thermal decomposition occurring under ramp heating conditions (Fig. 5b cf. Fig. 2 and Fig. 4a). The OH-stretching bands corresponding with the 2:1 layer and interlayer sheets showed a linear, slight decrease in intensity until 500°C. A significant reduction in bands attributed to OH groups in the interlayer sheet was observed between 600 and 650°C. After heating at 700–800°C, only a single broad band near 3600 cm^{-1} was present as evidence of persisting OH arrangements in the 2:1 layer. A similar IR pattern for MtBl was observed following isothermal heating at 450°C for 48h.

Mössbauer spectroscopy

Figure 6 shows Mössbauer spectra obtained for MtBl before and after isothermal heating in various conditions. Using the Mössbauer parameter criteria described by Dyar et al. (2006) and Baron et al. (2017), neither in the raw chlorite, nor in the heated samples was tetrahedrally coordinated Fe^{3+} identified. The raw MtBl sample had three clearly discernible doublets assigned to octahedrally coordinated Fe^{2+} with the same isomer shift (IS) of 1.14 mm/s and quadrupole splitting (ΔE_Q) values of 2.4, 2.6, and 2.85 mm/s, and one doublet assigned to octahedrally coordinated Fe^{3+} with IS values 0.45 mm/s and a ΔE_Q of 0.56 mm/s (Dyar et al. 2006). Although the three known models for Fe^{2+} match the conventional assignment to three octahedral environments in the chlorite structure (*trans* M1 and *cis* M2 arrangements in the 2:1 layer and M3 in the interlayer sheet; M4 preferred by trivalent

cations), the same IS value does not allow for distinguishing the sites M2 and M3 (cf. Smyth et al. 1997; Lougear et al. 2000).

The Mössbauer spectra of samples obtained after isothermal heating clearly showed that the relative area of the Fe^{3+} doublet increased above the 5% observed in unheated MtBl (Fig. 6, Tab. 3). The increase in the Fe^{3+} fraction with isothermal temperature, however, was not constant. Whereas the relative amount of Fe^{3+} increased with temperature and with time of isothermal heating up to 77%, the samples 450_24 and 450_48 reached a degree of Fe^{2+} oxidation lower than sample 400_48, 54% and 62%, respectively.

In addition to increasing the Fe^{3+} fraction, the quadrupole doublets of the Fe^{2+} and Fe^{3+} components also changed during heating. In samples isothermally heated at 350°C and 400°C for 24h, spectra were fitted using two Fe^{2+} components at the expense of increasing the Fe^{3+} components. Sample 400_48 could have been fitted adequately with only one Fe^{2+} doublet with parameters corresponding to those in untreated MtBl (IS 1.14 mm/s; ΔE_Q 2.6 mm/s), and with three new Fe^{3+} doublets. In contrast, samples heated at 450°C were fitted with three doublets of Fe^{2+} with significant variations in IS; average ΔE_Q of Fe^{2+} declined towards 2.2 mm/s, which indicates an increase in asymmetry of the Fe^{2+} sites (Gregori and Mercader 1994; Zanazzi et al. 2009). A new component with an IS of 1.05 mm/s and ΔE_Q at ~1.85 mm/s represents either tetrahedrally coordinated to oxygen or highly disordered Fe^{2+} (Burns and Solberg 1990; Dyar et al. 2006). In all isothermally heated samples, the Fe^{3+} component was identified in two or three different arrangements with ΔE_Q much greater than that in unheated MtBl, implying greater distortion of Fe^{3+} located in the newly formed environment (cf. Goodman and Bain 1979; Heller-Kallai and Rozenson 1981; Kodama et al. 1982).

Mössbauer spectra were obtained also for the final products of the heating of MtBl to 1000°C involving only ramp heating (10°/min_N2 and 20°/min_N2) or ramp heating with a 10°C min^{-1} rate preceded by the isothermal segment (DX_390_48) (Tab. 3). The ramp

conditions led to a slight oxidation of Fe^{2+} from 5% in the untreated material to 25% and 17% of Fe^{3+} for samples 10°/min_N2 and 20°/min_N2, respectively. Based on the criteria by Dyar et al. (2006), these ramp heated samples may contain a tetrahedrally coordinated Fe^{2+} component (IS ~0.9 mm/s; ΔE_Q ~2.2 mm/s) and a doublet that represents the delocalization of electrons between adjacent Fe^{3+} and Fe^{2+} (IS ~0.9 mm/s; ΔE_Q ~1.4 mm/s). Adding the step of prior isothermal heating at 390°C for 48h (DX_390_48 sample), the spectrum at 80K resulted in 13% of Fe^{2+} in a disordered environment similar to that for ramp heated samples (cf. Dyar et al. 2006), 10% of 6-coordinated Fe^{3+} and 77% of two magnetic Fe-O components. The development of two magnetic six-line spectra at 80K (Fig. 6) with a field of 46.0 T (small contribution) and 50.0 T (dominating contribution) indicated the presence of oxidized magnetite (Fe_3O_4), *i.e*. maghemite (γ-Fe_2O_3) (Murad 2010). None of the spectra showed evidence for the formation of goethite or hematite.

X-ray diffraction

After isothermal heating at elevated temperatures up to 450°C for 48 hours, a ~14-Å chlorite structure persisted and no newly-formed, non-chlorite phases were observed (Fig. 7, cf. Fig. 5). Except for a minor increase in unit cell dimensions, no significant changes were observed after 350ºC. However, after 24h and 48h isothermal heating at 400ºC, a new chlorite fraction with 001 at 13.91 Å appeared. This new 001 was distinguishably different from the 14.15 Å of the original chamosite and was the dominant reflection in sample 400_48. The 001 and 002 reflections of this secondary discrete phase are clearly distinguishable and their positions correspond to the rationality of the 00*l* reflection series. In turn, in samples 450_24 and 450_48, the 001 chlorite reflection became significantly broader and more intense, while the 002 reflection almost completely disappeared; in the 450_48 sample, the 002 peak was nearly absent.

After ramp heating to 1000°C (sample 10°C/min_N2), the cubic spinel phase such as ringwoodite $Fe^{2+}_{1.5}Mg_{0.5}SiO_4$ (COD 9001576), $Fe^{3+}MgAlO_4$ (COD 2310729), and forsterite $Fe_{0.935}Mg_{1.065}SiO_4$ (COD 9010754) were identified. Ramp heating following isothermal heating at 390°C for 48h (sample DX_390_48) produced similar cubic spinel phases but occurred simultaneously with maghemite γ-Fe_3O_4 (COD 9006317) or magnetite Fe_3O_4 (COD 1011032) (not distinguishable in diffractograms).

Discussion

Oxidative dehydrogenation

In oxygen-free conditions, where the mechanism of mass increase associated with oxygen incorporation may be tentatively neglected (see experiments under N_2 *vs.* air in Figs. 3 and 4a), any decrease in Δm_{dx} implies fewer OH groups available for dehydroxylation in order to remain consistent with Equations 1 and 2. Because mass loss upon theoretical dehydrogenation is nine times smaller than that upon dehydroxylation of the same environment, the contribution of dehydrogenation to Δm_{dx} is minimal. Therefore, the decline in Δm_{dx} shown in Figure 3 may be tentatively interpreted as evidence for dehydrogenation that occurred prior to dehydroxylation, hence reducing the OH content available for dehydroxylation. The extent of dehydrogenation increased with Fe(II) content in chlorite implying that dehydrogenation follows Equation 3, releasing hydrogen that forms H_2 (Steudel et al. 2016). According to Figure 3 showing series of chlorites and Figure 8a showing for Mg-chamosite, the slower the ramp heating rate, thus the longer the time at elevated temperature before dehydroxylation starts, the greater the dehydrogenation that precedes dehydroxylation. Adding an isothermal heating step can enhance dehydrogenation over dehydroxylation in chlorite (Tab. 2, Fig. 4a) in a similar manner as that observed in biotites and amphibolites oxidized during long-term heating (Rouxhet et al. 1972; Sanz et al. 1983) (cf. Borggaard et al.

1982; Rancourt et al. 2001). As shown in Figure 8a, Δm_{dx} matches the extent of Fe^{2+} oxidation determined by Mössbauer spectroscopy, providing at quantitative description of combined Equations 3 and 1.

The relationship in Figure 8a implies that the extent of dehydrogenation depends on the heating parameters such as rate, isothermal temperature, and time (cf. Scott and Amonette 1985; Rancourt et al. 2001). For all three tested chlorites differing in Fe^{2+} content, the longer the isothermal time, the smaller the Δm_{dx} for a given heating temperature (Tab. 2). However, the obtained results imply that to enhance dehydrogenation, the temperature of isothermal heating must be accurately defined (Fig. 8b). The greatest degree of dehydrogenation and smallest degree of dehydroxylation were observed after an isothermal run at a temperature just before the onset of dehydroxylation and was unique for each studied chlorite. For the Fe(II)-rich chlorite, MtBl, a narrow range of temperatures 390-410°C was favorable; any lower or higher temperatures than the optimum resulted in a lower amount of Fe^{3+} and a larger Δm_{dx}. However, temperatures required for the dehydrogenation of the other two clinochlores, (Sptb and CCC), were higher, and isothermal heating above 550°C and 500°C, respectively, or points when a minimum Δm_{dx} was noted, did not cause increased total mass loss (Tab. 2). Moreover, an excessively elevated temperature quickly removes a large portion of hydrogen by dehydroxylation, leaving little or no Fe^{2+}-linked hydroxyl hydrogen available for dehydrogenation, thus for Fe^{2+} oxidation. The reason why Borggaard et al. (1982) did not observe dehydrogenation under isothermal heating at 480°C can be explained by excessively low temperature selected for Fe-clinochlore heating. In this study, it is suggested that dehydrogenation in chlorite is a slow process that prefers isothermal or low-rate ramp heating in stark contrast to dehydroxylation, which occurs instantaneously. The same conclusion applied to annite studied by Rancourt et al. (2001), which may be considered an analogue of chlorite's 2:1 layer.

As shown in this study and previous studies on heat-treated chlorite (Goodman and Bain 1979; Steudel et al. 2016), no external oxygen is needed to oxidize structural Fe^{2+} (cf. Sanz et al. 1983). The fact that ramp heating of MtBl with a 20°C min^{-1} rate resulted in a Δm_{dx} closer to theoretical $H_2O(+)$ than any other TG experiment (Tab. 2), and left the highest Fe^{2+} fraction unaffected by oxidation (Tab. 3) implies that a dehydroxylation reaction alone does not lead to extensive dehydrogenation and Fe^{2+} oxidation. Only if isothermally-induced dehydrogenation is involved, Fe in the final product is strongly oxidized. Besides the formation of cubic Mg-Fe silicate and aluminate spinel phases observed after fast dehydroxylation of chamosite in the present study and in Steudel et al. (2016) (cf. MacKenzie and Bowden 1983; MacKenzie and Berezowski 1984 for amesite and berthierine), the dehydrogenation produced also maghemite. Dehydrogenation occurring in an inert gas atmosphere, therefore, returned the reaction's solid products similar to those obtained under oxidizing conditions, i.e. production of oxy-phases rather than amorphous products obtained during dehydroxylation (cf. Hodgson et al. 1965; Rouxhet et al. 1972). These observations disprove the notion that the dehydroxylation reaction itself oxidizes structural Fe^{2+} not only in chlorites (Villiéras et al. 1992) but also in all phyllosilicates (Heller-Kallai and Rozenson 1980; Scott and Amonette 1985).

The extent of Fe^{2+} oxidation reflects only the extent of dehydrogenation following Equation 3 (cf. Borggaard et al., 1982) and can be easily distinguished from the dehydroxylation reaction that follows Equation 2 (MacKenzie and Berezowski 1981; MacKenzie et al. 1986). Except for these two reactions, no other mechanism is needed to explain the mass loss and Fe^{2+} oxidation in thermally-treated chlorites under inert gas conditions (cf. Scott and Amonette 1985 and references therein). As dehydroxylation and dehydrogenation are governed by different mechanisms and kinetics, changing the heating

pattern leads to different oxidation states of the final product and different total mass loss, thus different quantities of released H_2O.

Quantitative assessment of dehydrogenation in relation to dehydroxylation

Although the extent of dehydrogenation can be measured by mass loss based solely on H release, this is difficult in a technical sense due to the overlap with dehydroxylation (cf. Borggaard et al. 1982). Based on evidence that dehydroxylation and dehydrogenation follow Equation 2 and Equation 3, respectively, the extent of dehydrogenation can be determined by measuring mass loss due to the dehydroxylation of OH groups remaining in a sample after dehydrogenation or by measuring the extent of Fe^{2+} oxidation. According to Equation 3, where one hydrogen atom must be lost for each Fe^{2+} atom oxidized under an inert gas atmosphere, calculations were performed for the studied chamosite sample (Tab. 4). The mass of released hydrogen (H_{Fe}, Tab. 4) was calculated using the Fe^{3+}content in isothermally heated specimens ($Fe^{3+}{}_N$) and reduced by the quantity of Fe^{3+} initially present in the sample (Tab. 3). For example, the oxidation of 72% of Fe^{2+} in the 400_48 specimen corresponded to a mass loss of 0.38 wt% due to hydrogen release during the isothermal step. Mass lost during the isothermal step (Δm_{iso}) reduced by H_{Fe} corresponds to mass lost only due to dehydroxylation during isothermal heating; the subtracted amount is taken as the mass of hydrogen involved in the dehydroxylation reaction (H_{dx}) for a direct comparison with H_{Fe}. The H_{Fe}/H_{dx} ratio, therefore, represents the quantitative ratio of dehydrogenation and dehydroxylation in the observed mass loss and allows to track the most favorable conditions for a particular reaction. For samples heated at 350°C, the overall extent of both reactions is small, but the ratio $H_{Fe}/H_{dx} > 1$ means that dehydroxylation is a minor event and isothermal conditions are preferred for dehydrogenation. At 400°C, H_{Fe}/H_{dx} is close to 1, hence both reactions are at an advanced stage, whereas at 450°C and for the ramp heated sample $H_{Fe}/H_{dx} < 1$ conditions are favorable for dehydroxylation to occur.

When compared with the total hydrogen mass in the sample, H_{Fe} and H_{dx} values can be used to estimate the relative ratio of unaltered (L_{ini}), dehydrogenated (L_{dh}), and dehydroxylated (L_{dx}) layers (cf. Drits et al. 2012b). Such an approach is biased due to oversimplification; for example, a given layer can have one altered sheet while the other sheet may remain unaltered or altered by another reaction; however, it may work as an approximation. Indeed, the formation of a discrete phase presenting its own 00l series (Fig. 7) corresponds to a high fraction of L_{dh} layers with a significant proportion of the original chlorite and a small fraction of dehydroxylated layers at 400°C (Tab. 4). The appearance of a population of dehydrogenated chlorite is attributed to $Fe^{3+}OH$ arrangements homogeneity in the chlorite layer accompanied by an increase in the quadrupole splitting (ΔE_Q) of the newly formed Fe^{3+} site, indicating its greater distortion in the new environment (Tab. 3). Higher isothermal temperature (450°C) and ramp heating produce a much larger fraction of L_{dx} layers and likely interstratification of all three types of layers. Following the conclusions of Drits et al. (2012) from the mixed-layered structure of partially-dehydroxylated illite, the broadening behavior of 00l reflections of MtBl heated isothermally at 450°C may correspond to an interstratified phase formed by the original chlorite layers as well as dehydroxylated and dehydrogenated (completely or partially) layers. A marked decrease in the ΔE_Q of Fe^{2+} component after heating at 450°C confirmed greater distortion of Fe^{2+} in the dehydroxylated environment (Tab. 3) (Zanazzi et al. 2009). The inhomogeneity of the OH state between the octahedral sheets most likely also contributes to the broadening of the 001 reflections and an increase in the I(001)/I(002) ratio. A similar phenomenon was also observed by Borggaard et al. (1982) for oxidized and reduced Fe-clinochlore and by Rancourt et al. (2001) for heated and dehydrogenated annite. In this study, it is suggested that the loss of homogeneity of the layer structure and the layers' interstratification are the reasons for the increased intensity of 001 and the decline of other *00l* reflections in chlorite heated at 550°C during the

588 conventional XRD-based test for chlorite identification test (Weiss and Rowland 1956;
589 Brindley and Chang 1974; Moore and Reynolds 1997).

590 **Dehydroxylation pathways in the context of dehydrogenation**

591 Considering the chemical composition and distribution of cations between two layers
592 according to the MtBl mineral formula, the most likely cation arrangements in the interlayer
593 (int) are $2Fe^{2+}AlOH$, $Fe^{2+}2AlOH$, and – less frequently – $3Fe^{2+}OH$, whereas in the octahedral
594 sheet of the 2:1 layer (2:1), they are as follows: $2Fe^{2+}MgOH$, $3Fe^{2+}OH$, and – less frequently
595 – $2Fe^{2+}VOH$ and $2MgFe^{2+}OH$ (*V* stands for vacancy). If dehydroxylation is the sole reaction
596 in the tested Mg-chamosite, then the thermal stability sequence thus the order of
597 dehydroxylation with increasing temperature is expected as follows (Brett et al. 1970;
598 Derkowski et al. 2012):

599 (int) $2AlFe^{2+}OH \approx$ (int) $2Fe^{2+}AlOH \approx$ (int) $3Fe^{2+}OH >$ (2:1) $V2Fe^{2+}OH >$ (2:1) $3Fe^{2+}OH >$
600 (2:1) $2Fe^{2+}MgOH >$ (2:1) $2MgFe^{2+}OH$ (5)

601 Fe-containing octahedral environments are most prone to dehydroxylation, both in
602 dioctahedral (Derkowski et al. 2012; Drits et al. 2012a) and trioctahedral phyllosilicates (Brett
603 et al. 1970; Mackenzie 1970; MacKenzie and Berezowski 1981). Apart from the type of
604 octahedral cations and their arrangements with respect to OH groups (Brett et al. 1970;
605 Mackenzie 1970), in chlorites, an additional factor, which also controls thermal stability is the
606 strength of bonding between the interlayer sheet and the 2:1 layer – the two are bound
607 together by both electrostatic and hydrogen-bonding forces (Nelson and Guggenheim 1993).
608 Weaker interlayer H-bonds are expected to dehydroxylate first, followed by stronger
609 interactions present in the 2:1 hydroxide sheet (Prieto et al. 1991; Zhan and Guggenheim
610 1995; Steudel et al. 2016).

611 Dehydrogenation as an oxidative reaction prefers arrangements enriched in Fe^{2+}
612 (Vedder and Wilkins 1969; Rancourt et al. 2001). For the prevailing local cation

arrangements of MtBl, dehydrogenation in an individual octahedral sheet can proceed as follows:

interlayer: $2Fe^{2+}Al(OH)_6 \rightarrow H^{\bullet}\uparrow+Fe^{2+}Fe^{3+}Al(OH)_5O \rightarrow H^{\bullet}\uparrow+2Fe^{3+}Al(OH)_4O_2$ (6)

2:1 layer: $2Fe^{2+}Mg(OH)_2O_4 \rightarrow H^{\bullet}\uparrow+Fe^{2+}Fe^{3+}Mg(OH)O_5 \rightarrow H^{\bullet}\uparrow+2Fe^{3+}MgO_6$ (7)

For Equation 7, a dehydrogenation reaction alone in the 2:1 layer environment can consume all OH groups potentially available for dehydroxylation, but it oxidizes only two out of a maximum of three Fe^{2+}, as in the case of annite (Rancourt et al. 2001). Hence, it is suspected that the disappearance of the high-temperature DTG peak when ramp heating a sample under oxidizing conditions is tentatively associated with complete dehydrogenation in the 2:1 layer of MtBl (Fig. 4b) before its dehydroxylation. The same thermal behavior identified on DTG patterns reflecting Equations 6 and 7 was observed under inert gas conditions for isothermally heated MtBl at a range of 390–410°C when dehydrogenation was enhanced (Fig. 4d). Indeed, almost complete dehydrogenation of the octahedral sheets of the 2:1 layer was accompanied by the reduction of OH-stretching bands ascribed to $2Fe^{2+}Mg$–OH and $2MgFe^{2+}$–OH arrangements in the 2:1 layer (Fig. 5a). In sample 400_48, oxidation reached 72% of total Fe, whereas the distribution of Fe between octahedral sheets was 45% in the interlayer and 55% in the 2:1 layer, hence, the dehydrogenation must have involved also Fe^{2+}OH at interlayer octahedral locations. When the progress of dehydrogenation prevails over dehydroxylation (Tab. 4, $L_{dh}/L_{dx} > 2$), the formation of Fe^{3+}OH environments in the interlayer (Eq. 6) can be observed after isothermal heating at 350°C as the appearance of a new, low-temperature DTG peak at 490°C (29% of oxidized Fe^{2+}; Fig. 4c). The same magnitude of the DTG peak shift to a low temperature was observed during ramp heating of MtBl under synthetic air (Fig. 4b). The low temperature of this DTG effect suggests its origin in the dehydroxylation of the $3Fe^{3+}$OH and/or $2Fe^{3+}$AlOH arrangements formed by dehydrogenation occurring in the interlayer (Eq. 6). Furthermore, a slight reduction in the high-temperature DTG peaks (~660

and 720 °C) and the smoothing of the OH-stretching band close to 3625 cm^{-1} (Fig. 5a) (cf. Vedder and Wilkins 1969) may also correspond to a minor dehydrogenation in the 2:1 layer occurring at 350°C. These isothermal temperatures producing maximum dehydrogenation depend on the iron content in chlorite and may be related to crystallite thickness (cf. Rancourt et al. 2001) and the Fe^{2+} and Mg distribution between the two chlorite octahedral sheets (Goodman and Bain 1979).

In step-wise heating (thermo-DRIFT experiments), IR spectra of MtBl did not result in a distinguishable decomposition of the interlayer followed by the 2:1 layer (Fig. 5b). Some dehydroxylation of OH groups in the octahedral sheet of the 2:1 layer occurred until 500°C. A proceeding dehydrogenation can change the expected sequence given in Equation 5 and hence the expected 3:1 mass loss ratio during two thermal events (Eq. 2). Such variability was observed for ramp-heated Fe(II)-containing chlorites in this study (Fig. 2) as well as in early studies (Post and Plummer 1972; Prieto et al. 1991; Villiéras et al. 1993; Steudel et al. 2016). These findings seem to be in accordance with Villiéras et al. (1993) and Steudel et al. (2016) pointed that the idealized Equation 2 is correct only for iron-free clinochlores.

Implications

The thermal decomposition of all Fe(II)-bearing chlorites involves two distinct but overlapping reactions: dehydroxylation and oxidative dehydrogenation. Our study has shown that dehydroxylation does not lead to the oxidation of structural Fe^{2+}; instead, oxidation results only from the dehydrogenation reaction. Two different reactions, dehydroxylation and dehydrogenation, occur simultaneously during heating, but independently of each other following Equations 1 and 3, respectively. Each of these reactions prefers different arrangements of cations distributed between two octahedral sheets, and different reaction conditions in general.

Dehydrogenation does not lead to the breakdown of chlorite's structural coherence like dehydroxylation does (Borggaard et al. 1982; Villiéras et al. 1993; Zhan and Guggenheim 1995). In response to enhanced dehydrogenation involving both octahedral sheets, a discrete fraction of ferric (oxy)chamosite phase is formed. Both the dehydroxylation and dehydrogenation of chlorite produce an interstratified structure consisting of original, dehydroxylated, and dehydrogenated chlorite layers (cf. Drits et al. 2012b).

Due to high OH content, chlorite is one of the key mineral supplying H_2O to magmatic or metamorphic environments, particularly in subduction zones (cf. Grove et al. 2012; Manthilake et al. 2016); the actual quantity of "structural water" provided by chlorite can be, however, reduced by prior dehydrogenation. The predicted degree of maximum $H_2O(+)$ reduction depends on Fe(II) content in a chlorite structure. Whereas the ideal $H_2O(+)$ remains essentially unchanged for Fe(II)-free chlorite, the quantity of "structural water" transported by end-member chamosite can theoretically drop even to 50% if advanced dehydrogenation occurs before dehydroxylation. The most enhanced dehydrogenation that was found in our study for Mg-chamosite (72% of oxidized structural Fe^{2+}) caused a reduction by 28% of total released H_2O. Because chlorite is the major H_2O- -supplying mineral in a subducted slab, an extreme case such as chamosite means that H_2O transported to a mantle wedge can be significantly reduced (cf. Grove et al. 2012). It is to be found whether the dehydrogenation reaction can contribute to H_2 produced in deep geologic formations (Berndt et al. 1996).

Chlorite composition is commonly used in geothermometry of diagenetic, hydrothermal, and metamorphic environments (eg., Inoue et al. 2009; Vidal et al., 2006). Fe^{3+} *vs.* Fe^{2+} content is an especially sensitive parameter in determining paleotemperature, pressure, and oxygen activity (Vidal et al., 2016). The presence of Fe^{3+} resulting from dehydrogenation would greatly affect the estimation of paleoenvironmental parameters, which are based on an assumption that chlorite composition preserves the crystallization conditions.

Based on the models summary presented by Lanari et al. (2014) or Vidal et al. (2016), only 20% of structural Fe^{2+} oxidation would result in paleotemperature underestimation by 150°C, whereas 40% oxidation would either decrease the temperature by > 250°C or shift the studied chlorite to a different redox realm. Because the calculation of chlorite chemical formula assumes complete OH occupation, dehydrogenation virtually changes the cations' distribution, increasing the number of octahedral vacancies and tetrahedral Al. The maximum degree of dehydrogenation (while tentatively excluding dehydroxylation) in MtBl would produce the formula as: $[Fe^{2+}_{0.82}Mg_{0.92}Mn_{0.08}Al_{1.33}Fe^{3+}_{2.75}\square_{0.10}](Si_{2.65}Al_{1.35})\ O_{18}H_{5.44}]$. Release of one hydrogen atom per one oxidized Fe(II) allows to maintain the charge balance. If dehydrogenation is not taken into account, the calculation of mineral formula that assumes complete hydroxyls occupancy $(OH)_8$ would be $[Fe^{2+}_{0.75}Mg_{0.85}Mn_{0.07}Al_{0.89}Fe^{3+}_{2.50}\square_{0.93}](Si_{2.42}Al_{1.575})\ O_{10}(OH)_8]$. Considering the degree of oxidative dehydrogenation recorded in the studied MtBl sample, the vacancy-based geothermometry results in temperature underestimation by hundreds °C (Vidal et al. 2006, 2016), whereas the Al^{IV} would make an overestimation by up to 150°C (Inoue et al. 2009). Although this is an extreme and likely impossible in nature case, potentially, even minor dehydrogenation can invalidate any chlorite geothermometry model.

Fe(III) content in natural chlorite is generally limited to 1 a.p.f.u. of Trincal and Lanari (2016) discussed the end-member having in 2 Fe(III) a.p.f.u. Our study proves that a dehydrogenated chlorite can accommodate such high Fe(III) content, even in a tri-, trioctahedral structure. As present chlorite-based geothermometry models are limited to 1 Fe(III) a.p.f.u. (Vidal et al. 2016), and new models involving Fe(III) > 1 a.p.f.u. are to be considered, the obtained 2.75 can represent the experimentally-proven uppermost limit given that dehydrogenation is considered.

712 The present study reveals the mechanism of dehydrogenation, conditions required to
713 proceed, and its product. It is, however, to be found to what extent (if any) dehydrogenation
714 of chlorite occurs in natural environment, what is its kinetics, and whether the
715 dehydrogenated structure persists over geological time. Whereas dehydroxylation of
716 trioctahedral phyllosilicates is irreversible (due to a layer structure collapse), reversibility of
717 dehydrogenation (oxidation) has been observed in chlorite (Borggaard et al. 1982) and biotite
718 (Farmer et al. 1971) when heating under H_2 gas.
719

720 **Acknowledgments**

721 The authors would like to thank Professor Gary J. Long for an immensely useful discussion
722 on Mössbauer spectroscopy results and Dr. Marek Szczerba for his valuable comments.
723 Vincent Trincal's review greatly helped to improve the Implications.
724

References

Bai, T.B., Guggenheim, S., and Wang, S.J. (1993) Metastable phase relations in the chlorite-H_2O system. American Mineralogist, 78, 1208–1216.

Baron, F., Petit, S., Pentrák, M., Decarreau, A., and Stucki, J.W. (2017) Revisiting the Nontronite Mössbauer Spectra. American Mineralogist, 102, 1501–1515.

Bayliss, P. (1975) Nomenclature of the Trioctahedral Chlorites. Canadian Mineralogist, 13, 178–180.

Berndt, M.E., Allen, D.E., and Seyfried, W.E. (1996) Reduction of CO_2 during serpentinization of olivine at 300 degrees C and 500 bar. Geology, 24, 351–354.

Bishop, J.L., Lane, M.D., and Dyar, M.D. (2008) Reflectance and emission spectroscopy study of four groups of phyllosilicates: smectites, kaolinite-serpentines, chlorites and micas. Clay Minerals, 43, 35–54.

Borggaard, O.K., Lindgreen, H.B., and Morup, S. (1982) Oxidation and Reduction of Structural Iron in Chlorite at 480°C. Clays and Clay Minerals, 30, 353–363.

Bourdelle, F., Parra, T., Chopin, C., and Beyssac, O. (2013) A new chlorite geothermometer for diagenetic to low-grade metamorphic conditions. Contributions to Mineralogy and Petrology, 165, 723–735.

Brett, N.H., MacKenzie, K.J.D., and Sharp, J.H. (1970) The thermal decomposition of hydrous layer silicates and their related hydroxides. Quarterly Reviews, Chemical Society, 24, 185–207.

Brindley, G.W., and Chang, T.S. (1974) Development of long basal spacings in chlorites by thermal treatment. American Mineralogist, 59, 152–158.

Brindley, G.W., and Youell, R.F. (1952) Ferrous chamosite and ferric chamosite. Mineralogical Magazine, 37, 57–70.

Burns, R.G., and Solberg, T.C. (1990) Chapter IV. Fe-Bearing Oxide, Silicate, and Aluminosilicate Minerals Crystal Structure Trends in Mössbauer. In Spectroscopic Characterization of Minerals and Their Surfaces. pp. 262–283.

Deer, W.A., Howie, R.A., and Zussman, J. (1992) An Introduction to the Rock Forming Minerals, 340-343 p. Longman, Harlow.

Derkowski, A., Drits, V.A., and McCarty, D.K. (2012) Nature of rehydroxylation in dioctahedral 2:1 layer clay minerals. American Mineralogist, 97, 610–629.

Drits, V.A., Besson, G., and Muller, F. (1995) An improved model for structural transformations of heat-treated aluminous dioctahedral 2:1 layer silicates. Clays and Clay Minerals, 43, 718–731.

759 Drits, V.A., Derkowski, A., and McCarty, D.K. (2012a) Kinetics of partial dehydroxylation in
760 dioctahedral 2:1 layer clay minerals. American Mineralogist, 97, 930–950.
761 Drits, V.A., McCarty, D.K., and Derkowski, A. (2012b) Mixed-layered structure formation
762 during trans-vacant Al-rich illite partial dehydroxylation. American Mineralogist, 97,
763 1922–1938.
764 Dyar, M.D., Agresti, D.G., Schaefer, M.W., Grant, C.A., and Sklute, E.C. (2006) Mössbauer
765 Spectroscopy of Earth and Planetary Materials. The Annual Review of Earth and
766 Planetary Science, 34, 83–125.
767 Farmer, V.C., Russell, J.D., McHardy, W.J., Newman, A.S.D., Ahlrichs, J.L., and Rimsaite,
768 J.Y.H. (1971) Evidence for loss of protons and octahedral iron from oxidized biotites and
769 vermiculites. Mineralogical Magazine, 38, 121–137.
770 Foster, M.D. (1962) Interpretation of the composition and a classification of the chlorites.
771 U.S. Geological Survey Professional Paper, 414–A, 1–33.
772 Goodman, B.A., and Bain, D.C. (1979) Mössbauer spectra of chlorites and their
773 decomposition products. Developments in Sedimentology, 27, 65–74.
774 Górnicki, R., Artur, B., and Ruebenbauer, K. (2007) Mössbauer Spectrometer MsAa-3.
775 Nucleonika, 52, 1–8.
776 Grazulis, S., Chateigner, D., Downs, R.T., Yokochi, A.F.T., Quirós, M., Lutterotti, L.,
777 Manakova, E., Butkus, J., Moeck, P., and Le Bail, A. (2009) Crystallography Open
778 Database - an open-access collection of crystal structures. Journal of Applied
779 Crystallography, 42, 726–729.
780 Gregori, D.A., and Mercader, R.C. (1994) Mössbauer study of some Argentinian chlorites.
781 Hyperfine Interactions, 83, 495–498.
782 Grove, T.L., Till, C.B., and Krawczynski, M.J. (2012) The Role of H_2O in Subduction Zone
783 Magmatism. Annual Review of Earth and Planetary Sciences, 40, 413–439.
784 Guggenheim, S., and Zhan, W. (1999) Crystal structures of two partially dehydrated chlorites:
785 The “modified” chlorite structure. American Mineralogist, 84, 1415–1421.
786 Guggenheim, S., Vhang, Y.-H., and Koster Van Groos, A., F. (1987) Muscovite
787 dehydroxylation : High Temprature Studies. American Mineralogist, 72, 537–550.
788 Hayashi, H., and Oinuma, K. (1967) Si-O absorption band near 1000 cm^{-1} and OH absorption
789 bands of chlorite. The American Mineralogist, 52, 1206–1210.
790 Heller-Kallai, L., and Rozenson, I. (1980) Dehydroxylation of dioctahedral phyllosilicates.
791 Clays and Clay Minerals, 28, 355–368.
792 ——— (1981) The use of Mössbauer spectroscopy of iron in clay mineralogy. Physics and

Chemistry of Minerals, 7, 223–238.

Heller-Kallai, L., Miloslavski, I., and Grayevsky, A. (1989) Evolution of hydrogen on dehydroxylation of clay minerals. American Mineralogist, 74, 1976–1978.

Hodgson, A.A., Freeman, A.G., and Taylor, H.F.W. (1964) The thermal decomposition of crocidolite from Koegas, South Africa. Journal of the Chemical Society, 35, 5–30.

——— (1965) The thermal decomposition of amosite. Mineralogocal Magazine, 35, 446–463.

Hogg, C.S., and Meads, R.E. (1975) A Mössbauer study of thermal decomposition of biotites. Mineralogical Magazine, 40, 79–88.

Inoue, A., Meunier, A., Patrier-Mas, P., Rigault, C., Beaufort, D., and Viellard, P. (2009) Application of chemical geothermometry to low-temperature trioctahedral chlorites. Clays and Clay Minerals, 57, 371–382.

Kodama, H., Longworth, G., and Townsend, M.G. (1982) A Mössbauer investigation of some chlorites and their oxidation products. Canadian Mineralogist, 20, 585–592.

Lanari, P., Wagner, T., and Vidal, O. (2014) A thermodynamic model for di-trioctahedral chlorite from experimental and natural data in the system MgO-FeO-Al_2O_3-SiO_2-H_2O: Applications to P-T sections and geothermometry. Contributions to Mineralogy and Petrology, 167, 1–19.

Lougear, A., Grodzicki, M., Bertoldi, C., Trautwein, A.X., Steiner, K., and Amthauer, G. (2000) Mössbauer and molecular orbital study of chlorites. Physics and Chemistry of Minerals, 27, 258–269.

MacKenzie, K.J.D., and Berezowski, R.M. (1981) Thermal and Mössbauer studies of iron-containing hydrous silicates. I. Cronstedtite. Thermochimica Acta, 44, 171–187.

——— (1984) Thermal and Mössbauer studies of iron-containing hydrous silicates. V.Berthierine. Thermochimica Acta, 74, 291–312.

MacKenzie, K.J.D., and Bowden, M.E. (1983) Thermal and Mössbauer studies of iron-containing hydrous silicates. VI.Amesite. Thermochimica Acta, 64, 83–106.

MacKenzie, K.J.D., Berezowski, R.M., and Bowden, M.E. (1986) Thermal and Mössbauer studies of iron-containing hydrous silicates. VI. Minnesotaite. Thermochimica Acta, 99, 273–289.

Mackenzie, R.C. (1970) Differential Thermal Analysis. Volume 1. 18. Simple Phyllosilicates Based on Gibbsite- and Brucite-like Sheet, 512-517 p.

Manthilake, G., Bolfan-Casanova, N., Novella, D., Mookherjee, M., and Andrault, D. (2016) Dehydration of chlorite explains anomalously high electrical conductivity in the mantle

827 wedges. Science Advances, 2, 1–5.
828 Moore, D.M., and Reynolds, R.C. (1997) X-Ray Diffraction and the identification and
829 analysis of Clay Minerals, 233-235 p. Oxford University Press, U.K.
830 Murad, E. (2010) Mössbauer spectroscopy of clays, soils and their mineral constituents. Clay
831 Minerals, 45, 413–430.
832 Nelson, D.O., and Guggenheim, S. (1993) Inferred limitations to the oxidation of Fe in
833 chlorite: a high-temperature single-crystal X-ray study. American Mineralogist, 78,
834 1197–1207.
835 Post, J.L., and Plummer, C.C. (1972) The chlorite series of Flagstaff Hill area, California: A
836 preliminary investigation. Clays and Clay Minerals, 20, 271–283.
837 Prieto, A.C., Lobon, J.M., Alia, J.M., Rull, F., and Martin, F. (1991) Thermal and
838 spectroscopic analysis of natural trioctahedral chlorites. Journal of Thermal Analysis, 37,
839 969–981.
840 Rancourt, D.G., Mercier, P.H.J., Cherniak, D.J., Desgreniers, S., Kodama, H., Robert, J.L.,
841 and Murad, E. (2001) Mechanisms and crystal chemistry of oxidation in annite:
842 resolving the hydrogen-loss and vacancy reactions. Clays and Clay Minerals, 49, 455–
843 491.
844 Rouxhet, P., Gillard, J., and Fripiat, J. (1972) Thermal decomposition of amosite, crocidolite,
845 and biotite. Mineralogical Magazine, 38, 583–592.
846 Sanz, J., González-Carreño, T., and Gancedo, R. (1983) On dehydroxylation mechanisms of a
847 biotite in vacuo and in oxygen. Physics and Chemistry of Minerals, 9, 14–18.
848 Scott, A.D., and Amonette, J. (1985) Chapter 16. Role of iron in mica weathering. In Iron in
849 Soils and Clay Minerals. pp. 537–610.
850 Shirozu, H. (1980) Cation distribution, sheet thickness, and O-OH space in trioctahedral
851 chlorites- an X ray and infrared study. Mineralogical Journal, 10, 14–34.
852 ——— (1985) Infrared spectra of trioctahedral chlorites in relation to chemical composition.
853 Clay Science, 176, 167–176.
854 Smyth, J.R., Dyar, M.D., May, H.M., Bricker, O.P., and Acker, J.G. (1997) Crystal structure
855 refinement and Mössbauer spectroscopy of an ordered, triclinic clinochlore. Clays and
856 Clay Minerals, 45, 544–550.
857 Steudel, A., Kleeberg, R., Koch, C.B., Friedrich, F., and Emmerich, K. (2016) Thermal
858 behavior of chlorites of the clinochlore-chamosite solid solution series: Oxidation of
859 structural iron, hydrogen release and dehydroxylation. Applied Clay Science, 132–133,
860 626–634.

Trincal, V., and Lanari, P. (2016) Al-free di-trioctahedral substitution in chlorite and a ferri-sudoite end- member.

Vedder, W., and Wilkins, R. (1969) Dehydroxylation and Rehydroxylation, Oxidation and Reduction of Mica. American Mineralogist, 54, 482–509.

Vidal, O., Parra, T., and Trotet, F. (2001) A thermodynamic model for Fe-Mg aluminous chlorite using data from phase equilibrium experiments and natural pelitic assemblages in the 100° to 600°C, 1 to 25 kb range. American Journal of Science, 301, 557–592.

Vidal, O., De Andrade, V., Lewin, E., Munoz, M., Parra, T., and Pascarelli, S. (2006) P-T-deformation-Fe^{3+}/Fe^{2+} mapping at the thin section scale and comparison with XANES mapping: Application to a garnet-bearing metapelite from the Sambagawa metamorphic belt (Japan). Journal of Metamorphic Geology, 24, 669–683.

Vidal, O., Lanari, P., Munoz, M., Bourdelle, F., and de Andrade, V. (2016) Deciphering temperature, pressure and oxygen-activity conditions of chlorite formation. Clay Minerals, 51, 615–633.

Villiéras, F., Tvon, J., Cases, J.M., Zimmermann, J.L., and Baeza, R. (1992) Dosage et localisation du fer II dans le talc et la chlorite par analyse apectrometrique des gaz de thermolyse. Comptes Rendus de l'Académie des Sciences Paris, 315, 1201–1206.

Villiéras, F., Yvon, J., François, M., Maurice Cases, J., Lhote, F., and Uriot, J.P. (1993) Micropore formation due to thermal decomposition of hydroxide layer of Mg-chlorites: interactions with water. Applied Clay Science, 8, 147–168.

Villiéras, F., Yvon, J., Cases, J.M., De Donato, P., Lhote, F., and Baeza, R. (1994) Development of microporosity in clinochlore upon heating. Clays and Clay Minerals, 42, 679–688.

Wang, D., Yi, L., Huang, B., and Liu, C. (2015) High-temperature dehydration of talc: A kinetics study using in situ X-ray powder diffraction. Phase Transitions, 88, 560–566.

Weiss, E.J., and Rowland, R.A. (1956) Oscillating-heating X-ray diffractometr studies of clay mineral dehydroxylation. American Mineralogist, 41, 117–126.

Zanazzi, P.F., Comodi, P., Nazzareni, S., and Andreozzi, G.B. (2009) Thermal behaviour of chlorite: an in situ single-crystal and powder diffraction study. European Journal of Mineralogy, 21, 581–589.

Zhan, W., and Guggenheim, S. (1995) The dehydroxylation of chlorite and the formation of topotactic product phases. Clays and Clay Minerals, 43, 622–629.

Figures captions

Figure 1. Protocol for isothermal heating experiments: a – thermal equilibrium at 200°C for 10 minutes, b – isothermal heating for 1, 12, 24 or 48 hours at temperatures 350 – 625°C, c – ramp heating to 1000°C at 10°C min^{-1}, d – isothermal heating for 15 min at 1000°C, in some samples combined with changing the N_2 purge gas to synthetic air; m_0, m_{izo}, m_{ramp}, m_{min} and m_{air} points indicating masses used in calculations; gray dots indicate sampling points for *ex-situ* analyses.

Figure 2. TG and DTG patterns of ramp-heated tri-, trioctahedral chlorites (CCC, Sptb, and MtBl, see Table 1); rate of 10°C min^{-1} to 1000°C in N_2 gas atmosphere followed by a change to air at 1000°C for 15 minutes.

Figure 3. Mass loss (Δm_{dx}) recorded in various ramp heating conditions (in N_2 with 5, 10 and 20°C min^{-1} heating rates, in air with 5°C min^{-1} rate) and also theoretical mass loss upon total dehydroxylation, $H_2O(+)$, plotted as a function of Fe(II) content in seven studied tri-, trioctahedral chlorites.

Figure 4. TG patterns of Mg-chamosite (MtBl) heated isothermally followed by a ramp heating with 10°C min^{-1} rate to 1000°C under N_2 and air gas; then kept isothermally for 15 min at 1000°C under synthetic air (**a**); DTG patterns from: ramp heating only with 10°C min^{-1} rate to 1000°C under N_2 and synthetic air (**b**), ramp-heating after different isothermal steps, at 350-375°C (**c**), 390-410°C (**d**) and 425-475°C (**e**), under N_2.

Figure 5. OH stretching region of IR spectra of Mg-chamosite (MtBl) before and after heating experiments. Transmission spectra of MtBl *ex-situ* measured after different stages of isothermal heating experiments (**a**).Thermo-DRIFT spectra of MtBl sample heated *in-situ* up to 800°C (**b**). Transmission spectra were adjusted using a linear baseline.

Figure 6. Mössbauer spectra of untreated and heated Mg-chamosite (MtBl) following various isothermal heating experiments, and obtained after heating to 1000°C involving only ramp heating with 10 and 20°C min^{-1} rates (10°C/min_N2, 20°C/min_N2) analyzed at 300K. A spectrum of MtBl isothermally heated at 390°C for 48 h followed by ramp heating to 1000°C (DX_390_48_80K) was analyzed at 80K.

Figure 8. Relationship between structural Fe(III) and experimental total mass loss Δm_{dx} for selected measurements of Mg-chamosite (MtBl) (**a**) and correlation between experimental total mass loss (black) and the Fe^{2+} fraction (gray) for selected experiments with isothermal heating (**b**). (*) TG analytical problem at high-temperature end.

Figure 7. 001 and 002 reflections of XRD patterns for Mg-chamosite (MtBl) analyzed *ex-situ* before and after selected isothermal heating experiments. (*) Peak intensities are out of scale.

This is a preprint, the final version is subject to change, of the American Mineralogist (MSA)
Cite as Authors (Year) Title. American Mineralogist, in press.
DOI: https://doi.org/10.2138/am-2018-6541

931 **Tables**

932 **Table 1.** EPMA-based chemical composition of chlorites samples.

	MtBl n=25	Sptb n=29	CCC n=22
		wt%	
C total	b.d.l	b.d.l	0.6 ± 0.1
SiO_2	23.79 ± 0.25	28.03 ± 0.20	30.23 ± 0.426
Al_2O_3	20.49 ± 0.29	20.39 ± 0.19	19.79 ± 0.493
FeO	36.29 ± 0.52	16.00 ± 0.24	5.495 ± 0.22
Fe_2O_3	2.12 ± 0.03	1.135 ± 0.17	1.62 ± 0.06
Cr_2O_3	b.d.l.	b.d.l.	0.13 ± 0.04
MgO	5.58 ± 0.16	22.63 ± 0.24	31.01 ± 0.49
MnO	0.82 ± 0.08	0.12 ± 0.05	0.12 ± 0.04
NiO	b.d.l.	b.d.l	0.13 ± 0.03
TiO_2	0.025 ± 0.010	0.03 ± 0.01	0.05 ± 0.01
$H_2O(+)$	10.77	12.00	12.56
Total[a]	99.88	100.33	101.025
		a.p.f.u.	
Si	2.65 ± 0.02	2.78 ± 0.01	2.85 ± 0.03
Al^{IV}	1.35 ± 0.03	1.21 ± 0.02	1.15 ± 0.05
Al^{VI}	1.33 ± 0.03	1.18 ± 0.02	1.04 ± 0.05
Cr^{3+}	b.d.l.	b.d.l.	0.01 ± 0.004
Fe^{3+}	0.19 ± 0.002	0.085 ± 0.01	0.115 ± 0.005
Fe^{2+}	3.38 ± 0.04	1.33 ± 0.01	0.43 ± 0.02
Mg	0.92 ± 0.03	3.35 ± 0.03	4.35 ± 0.06
Mn	0.08 ± 0.007	0.01 ± 0.004	0.01 ± 0.004
Ni	b.d.l.	b.d.l.	0.01 ± 0.002
Fe/(Fe+Mg)	0.793±0.005	0.296±0.005	0.112±0.004

933 [a] sum without C total

934 Notes: All components were measured by using EPMA, except Fe(II)/ Fe(III) measured by
935 Mössbauer spectroscopy and C total measured by elemental chemical analysis (CHNS). b.d.l.
936 - below detection limit; n – number of analyses. Atoms per formula unit (a.p.f.u.) are
937 calculated on the basis of 14 oxygen atoms.

938

939 **Table 2.** Mass losses of tested Mg-chamosite (MtBl), Fe-clinochlore (Sptb), and clinochlore
940 (CCC) under various heating and gas atmosphere conditions. Each sample was dried *in-situ* in
941 a TG furnace isothermally for 10 min at 200°C before proceeding with the established heating
942 protocol and ramp-heated 10°C min^{-1} to 1000°C after the isothermal step.

Sample/ $H_2O(+)$	Sample type	Gas	Isothermal step		Δm_{dx} (wt%)	Δm_{iso} (wt%)	Δm_{ramp} (wt%)
			Temperature (°C)	Time (h)			
MtBl	**10°C/min_AIR**	Air	-	0	6.40	-	-
10.77 wt%	**20°C/min_N2**		-	0	10.50	-	-
	10°C/min_N2		-	0	10.06	-	-
	5°C/min_N2		-	0	9.83	-	-
	350_1		350	1	10.09	0.16	9.79
	350_12		350	12	9.57	0.38	9.07
	350_24[a]		350	24	9.06	0.49	8.45
	350_48[a]		350	48	9.25	0.56	8.56
	375_48		375	48	8.61	1.33	7.12
	390_48	N_2	390	48	7.81	3.28	4.36
	400_1		400	1	9.86	0.32	9.40
	400_12		400	12	9.36	1.37	7.84
	400_24[a]		400	24	8.96	2.35	6.36
	400_48[a]		400	48	7.80	4.17	3.44
	410_48		410	48	7.82	5.01	2.59
	425_48		425	48	8.39	5.40	2.73
	450_24[a]		450	24	8.90	6.22	2.39
	450_48[a]		450	48	8.42	7.18	0.95
	475_48		475	48	8.46	7.48	0.54
Sptb	**10°C/min_AIR**	Air	-	0	10.20	-	-
12.00 wt%	**20°C/min_N2**		-	0	11.50	-	-
	10°C/min_N2		-	0	11.50	-	-
	5°C/min_N2	N_2	-	0	11.17	-	-
	400_24		400	24	11.47	0.11	11.25
	450_24		450	24	11.43	0.18	11.13
	450_48		450	48	11.26	0.28	10.94
	475_48		475	48	11.29	2.42	8.77
	500_48		500	48	10.83	8.04	2.76
	525_48		525	48	10.85	8.10	2.61
	550_24		550	24	10.72	7.34	3.17
	550_48		550	48	10.47	8.09	2.33
	600_48		600	48	10.46	8.78	1.31

	625_48		625	48	10.51	8.43	1.20
CCC	**10°C/min_AIR**	Air	-	0	11.40	-	-
12.56 wt%	**20°C/min_N2**		-	0	12.50	-	-
	10°C/min_N2		-	0	12.45	-	-
	5°C/min_N2	N_2	-	0	12.15	-	-
	400_24		400	24	12.13	0.75	10.96
	400_48		400	48	11.90	0.90	10.70
	450_24		450	24	11.98	3.36	7.93
	450_48		450	48	11.95	4.68	7.09
	500_48		500	48	11.85	8.99	1.97
	525_48		525	48	11.69	8.93	1.67
	550_48		550	48	11.78	8.60	1.50

[a] samples used also in ex-situ analyses.

Notes: 20°C/min_N2, 10°C/min_N2 – samples ramp-heated with 20°C min^{-1} rate or 10 °C min^{-1} rate, respectively; Isothermal Temperature(°C)_Isothermal Time(h), e.g. 400_48– sample isothermally heated at 400°C for 48h, Δm_{dx} – total mass loss from 205°C to minimum mass; Δm_{iso} – mass loss corresponding to isothermal segment, Δm_{ramp} – mass loss corresponding to ramp-heating segment.

This is a preprint, the final version is subject to change, of the American Mineralogist (MSA)
Cite as Authors (Year) Title. American Mineralogist, in press.
DOI: https://doi.org/10.2138/am-2018-6541

950 **Table 3**. Fitted Mössbauer parameters for Mg-chamosite (MtBl) before and after various heating experiments.

Sample T(°C)_t(min)	Tempera-ture (°C)	Fe(II)				Fe(III)				Fe – O				
		IS (mm/s)	ΔE_Q (mm/s)	FWHM (mm/s)	I (%)	IS (mm/s)	ΔE_Q (mm/s)	FWHM (mm/s)	I (%)	IS (mm/s)	ΔE_Q (mm/s)	FWHM (mm/s)	I (%)	B (T)
MtBl	25	1.14	2.85	0.13	19(2)	0.45	0.56	0.34	5(1)					
		1.14	2.63	0.13	42(3)									
		1.14	2.39	0.25	34(2)									
350_24	25	1.15	2.66	0.15	52(8)	0.40	0.84	0.24	8(1)					
		1.05	2.62	0.24	26(4)	0.53	1.10	0.39	14(3)					
350_48	25	1.17	2.64	0.18	42(3)	0.44	0.87	0.31	17(1)					
		1.06	2.60	0.22	24(2)	0.39	1.46	0.44	17(2)					
400_24	25	1.15	2.63	0.18	38(2)	0.4	0.81	0.40	19(2)					
		1.01	2.55	0.28	11(2)	0.39	1.29	0.39	23(3)					
						0.35	1.87	0.35	9(2)					
400_48	25	1.14	2.60	0.23	23(3)	0.38	0.77	0.22	16(3)					
						0.37	1.20	0.30	37(6)					
						0.33	1.73	0.37	24(4)					
450_24	25	1.05	1.88	0.38	19(2)	0.37	1.11	0.39	38(2)					
		1.19	2.52	0.2	17(2)	0.42	1.61	0.41	16(3)					
		1.01	2.45	0.16	10(2)									
450_48	25	1.05	1.81	0.47	18(2)	0.40	1.07	0.38	41(2)					
		1.20	2.44	0.24	10(1)	0.39	1.66	0.41	21(2)					
		0.98	2.43	0.22	10(2)									
10°C/min_N2	25	1.13	2.11	0.27	29(2)	0.46	0.58	0.47	25(2)					
		1.20	2.59	0.25	19(1)									
		0.86[a]	1.33[a]	0.43[a]	19(1)[a]									
		0.82[b]	2.15[b]	0.15[b]	8(1)[b]									
20°C/min_N2	25	1.16	2.89	0.13	18(1)	0.43	0.63	0.49	17(1)					

		1.23	2.36	0.23	23(2)									
		0.93[a]	1.46[a]	0.44[a]	19(1)[a]									
		0.96[b]	2.29[b]	0.26[b]	23(2)[b]									
DX_390_48	25	0.75[a]	1.60[a]	0.98[a]	21(2)[a]	0.32	0.74	0.51	24(2)	0.55	-0.16	0.72	23(2)	40.8
										0.43	-0.01	0.72	32(3)	45.9
DX_390_48_80K	-193	0.94[a]	2.64[a]	1.10[a]	13(2)[a]	0.40	0.97	0.70	10(2)	0.70	-0.09	1.40	34(2)	46.0
										0.42	-0.02	0.56	43(2)	50.0

Notes: 10°C/min_N2– MtBl obtained after 10°C min^{-1} ramp heating to 1000°C; 10°C/min_N2 - MtBl obtained after 20°C min^{-1} ramp heating to 1000°C under nitrogen gas; DX_390_48 – MtBl obtained after isothermal heating segment at 390°C for 48h followed by ramp heating to 1000 °C under nitrogen gas.

[a] delocalization of electrons between adjacent Fe^{3+} and Fe^{2+} atoms resulting in an averaged value of IS that may be assigned to $Fe^{2.5+}$,

[b] tetrahedrally coordinated Fe^{2+} component (Dyar et al. 2006).

This is a preprint, the final version is subject to change, of the American Mineralogist (MSA)
Cite as Authors (Year) Title. American Mineralogist, in press.
DOI: https://doi.org/10.2138/am-2018-6541

Table 4. Calculation of hydrogen content evolved during the heating of Mg-chamosite (MtBl) based on thermogravimetric and Mössbauer spectroscopy results.

Sample	Δm_{dx} (wt%)	Δm_{iso} (wt%)	Δm_{ramp} (wt%)	$Fe^{3+}{}_N$ (wt%)	H_{Fe} (wt%)	H_{dx} (wt%)	H_{Fe}/H_{dx}	L_{ini} (%)	L_{dx} (%)	L_{dh} (%)
350_24	9.06	0.49	8.45	5.0	0.09	0.04	2.2	89	3	8
350_48	9.25	0.56	8.56	8.6	0.15	0.05	3.0	83	4	13
400_24	8.96	2.35	6.36	13.6	0.24	0.23	1.0	60	19	21
400_48	7.80	4.17	3.44	21.3	0.38	0.42	0.9	33	35	32
450_24	8.90	6.22	2.39	14.5	0.26	0.66	0.4	23	55	22
450_48	8.42	7.18	0.95	16.9	0.30	0.76	0.4	11	64	25

Notes: $Fe^{3+}{}_N$ - total measured Fe^{3+} reduced by Fe^{3+} content initially present in nascent MtBl; H_{Fe} – hydrogen released as a result of oxidative dehydrogenation during isothermal heating; H_{dx} – content of hydrogen released during dehydroxylation at the isothermal step; H_{Fe}/H_{dx} –proxy for dehydrogenation/dehydroxylation ratio during isothermal heating; L_{ini}, L_{dx}, L_{dh} - relative ratio of unaltered, dehydroxylated, and dehydrogenated layers, respectively.

This is a preprint, the final version is subject to change, of the American Mineralogist (MSA)
Cite as Authors (Year) Title. American Mineralogist, in press.
DOI: https://doi.org/10.2138/am-2018-6541

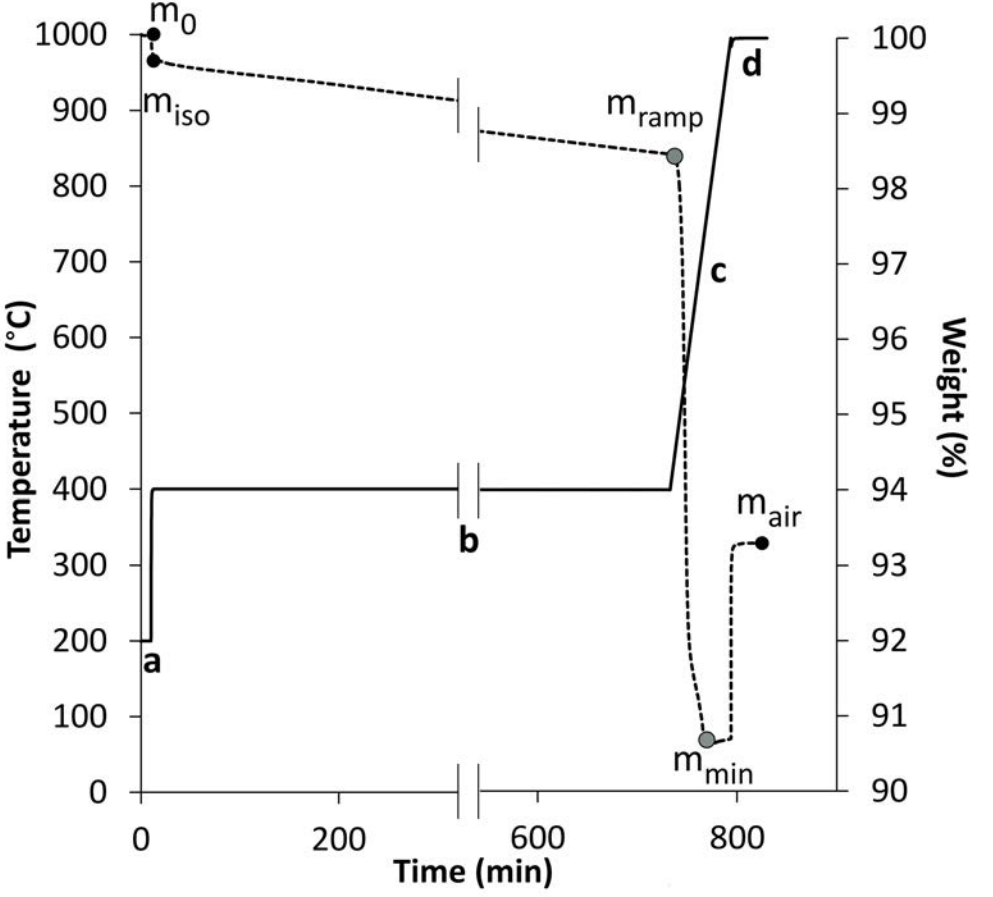

Figure 1

This is a preprint, the final version is subject to change, of the American Mineralogist (MSA)
Cite as Authors (Year) Title. American Mineralogist, in press.
DOI: https://doi.org/10.2138/am-2018-6541

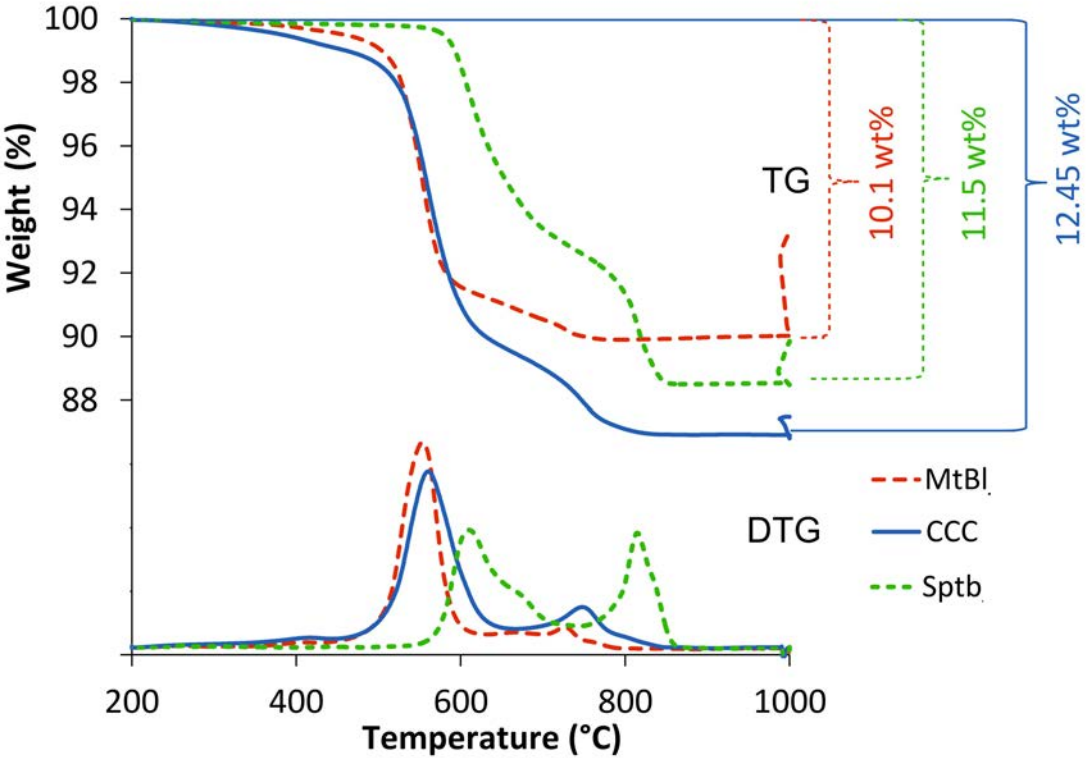

Figure 2

This is a preprint, the final version is subject to change, of the American Mineralogist (MSA)
Cite as Authors (Year) Title. American Mineralogist, in press.
DOI: https://doi.org/10.2138/am-2018-6541

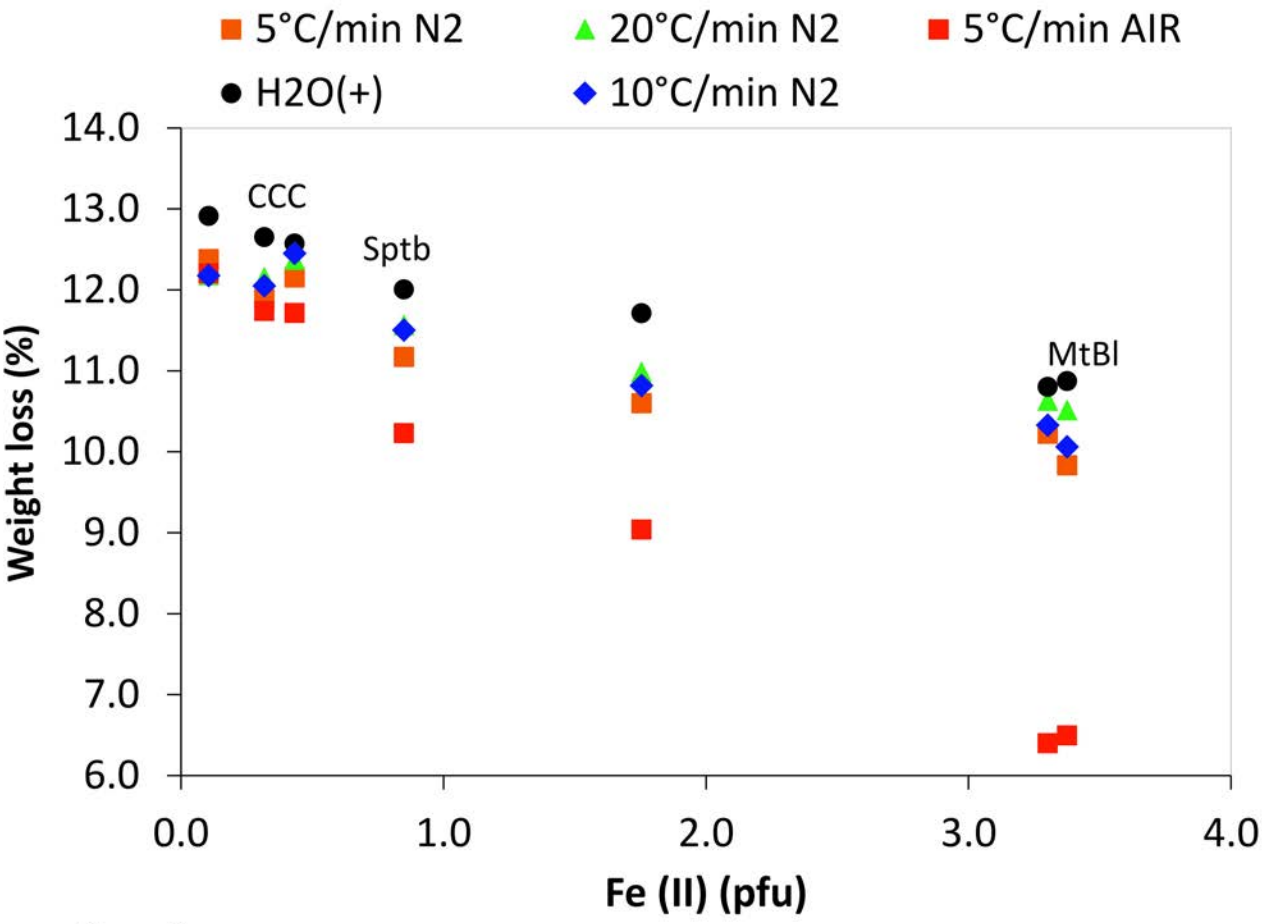

Figure 3

This is a preprint, the final version is subject to change, of the American Mineralogist (MSA)
Cite as Authors (Year) Title. American Mineralogist, in press.
DOI: https://doi.org/10.2138/am-2018-6541

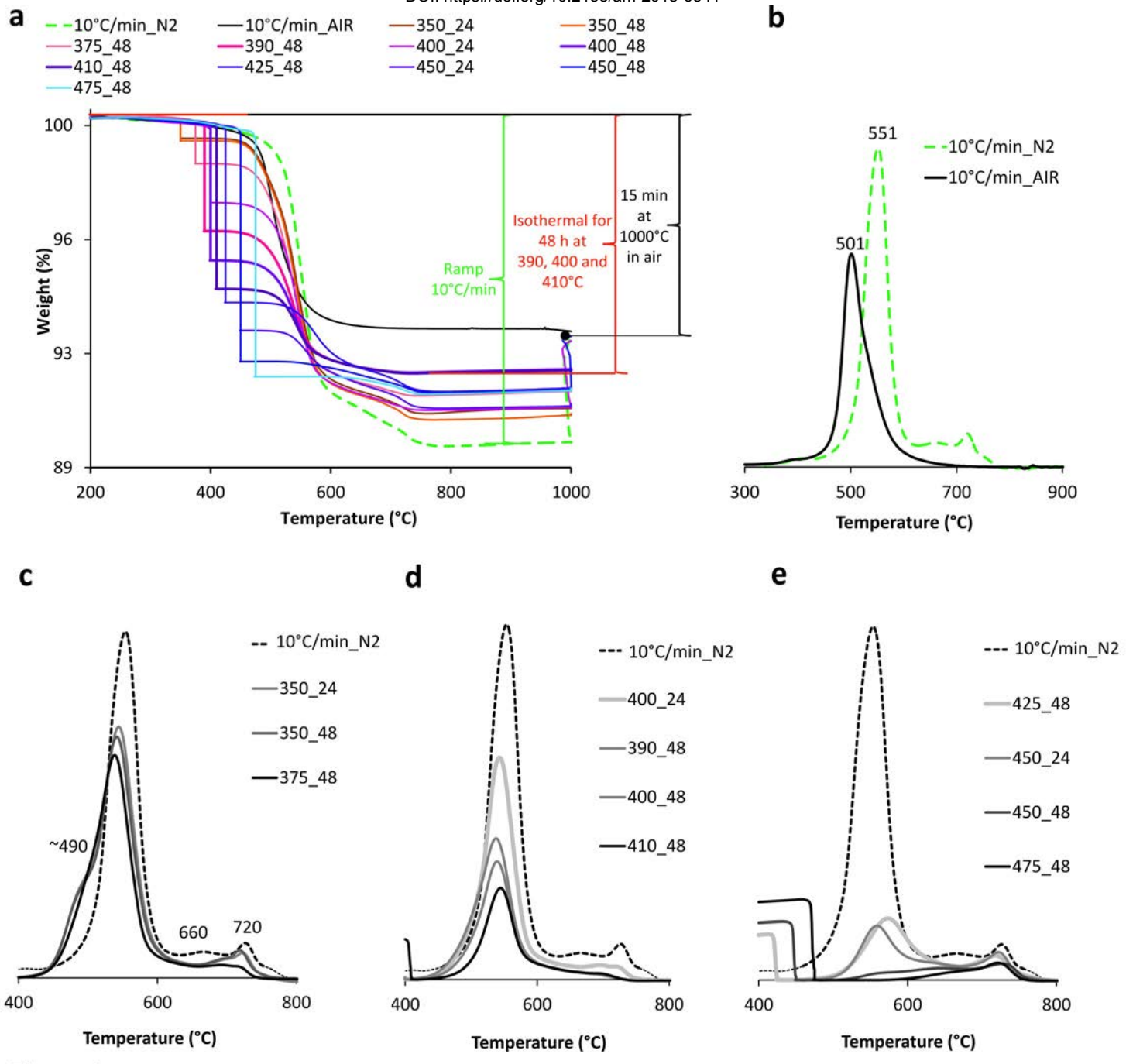

Figure 4

This is a preprint, the final version is subject to change, of the American Mineralogist (MSA)
Cite as Authors (Year) Title. American Mineralogist, in press.
DOI: https://doi.org/10.2138/am-2018-6541

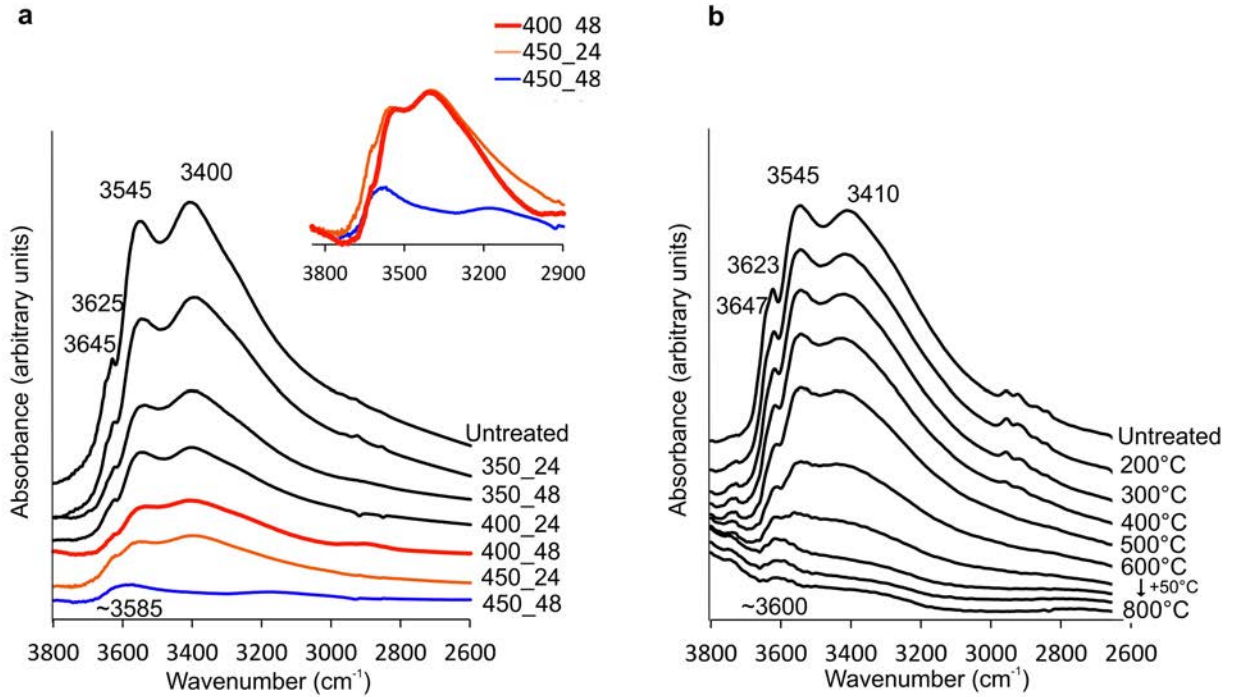

Figure 5

This is a preprint, the final version is subject to change, of the American Mineralogist (MSA)
Cite as Authors (Year) Title. American Mineralogist, in press.
DOI: https://doi.org/10.2138/am-2018-6541

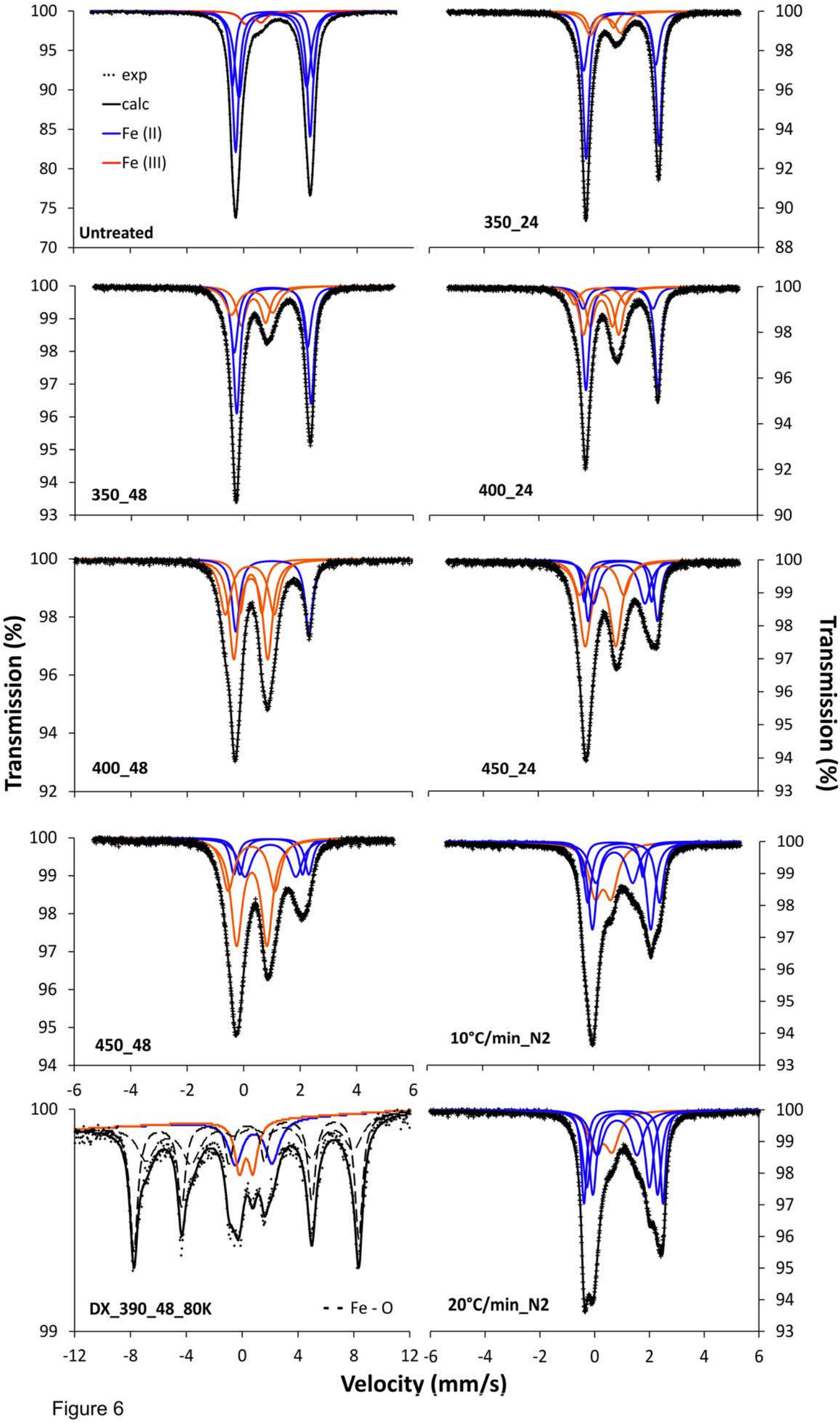

Figure 6

This is a preprint, the final version is subject to change, of the American Mineralogist (MSA)
Cite as Authors (Year) Title. American Mineralogist, in press.
DOI: https://doi.org/10.2138/am-2018-6541

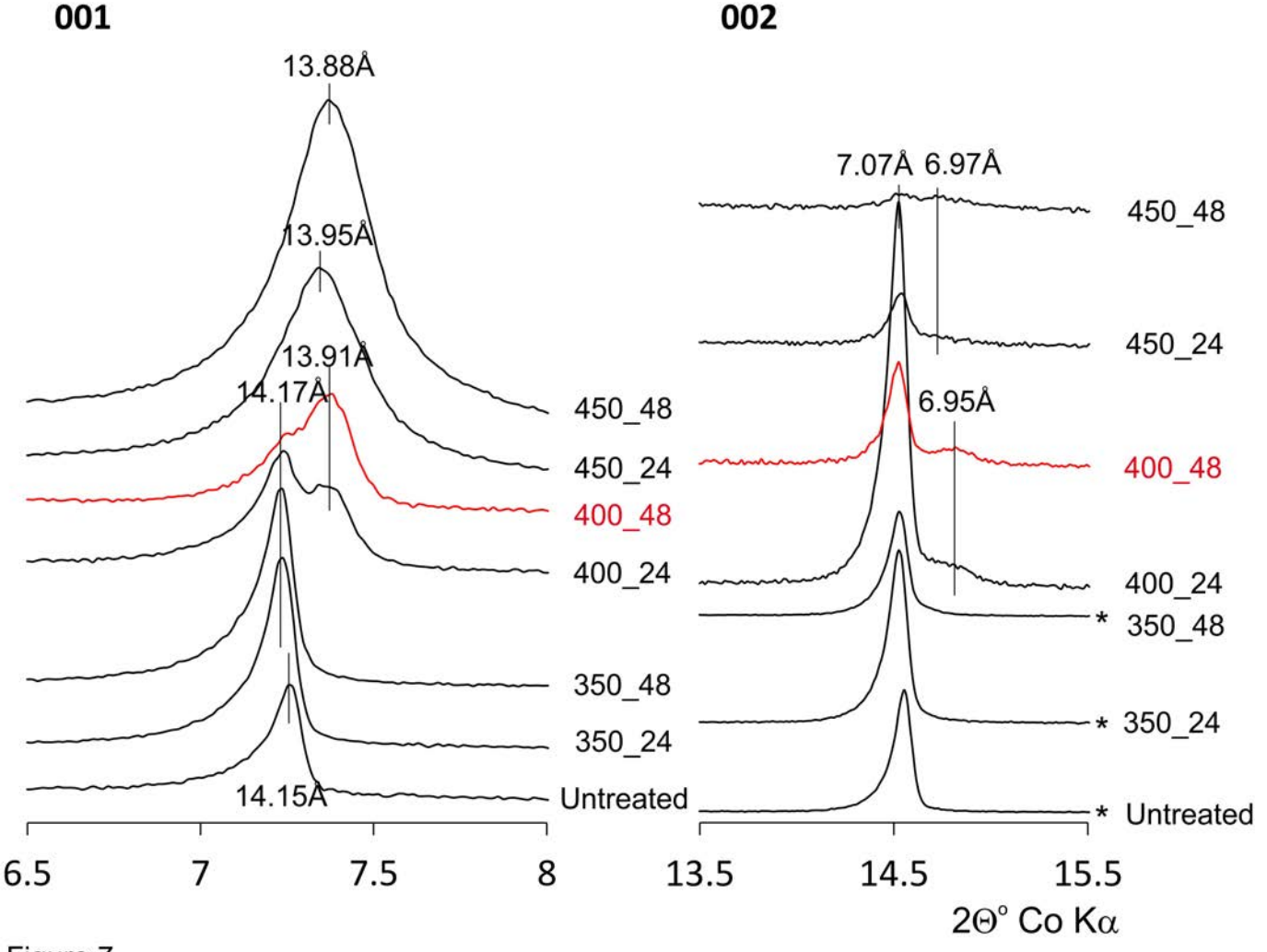

Figure 7

This is a preprint, the final version is subject to change, of the American Mineralogist (MSA)
Cite as Authors (Year) Title. American Mineralogist, in press.
DOI: https://doi.org/10.2138/am-2018-6541

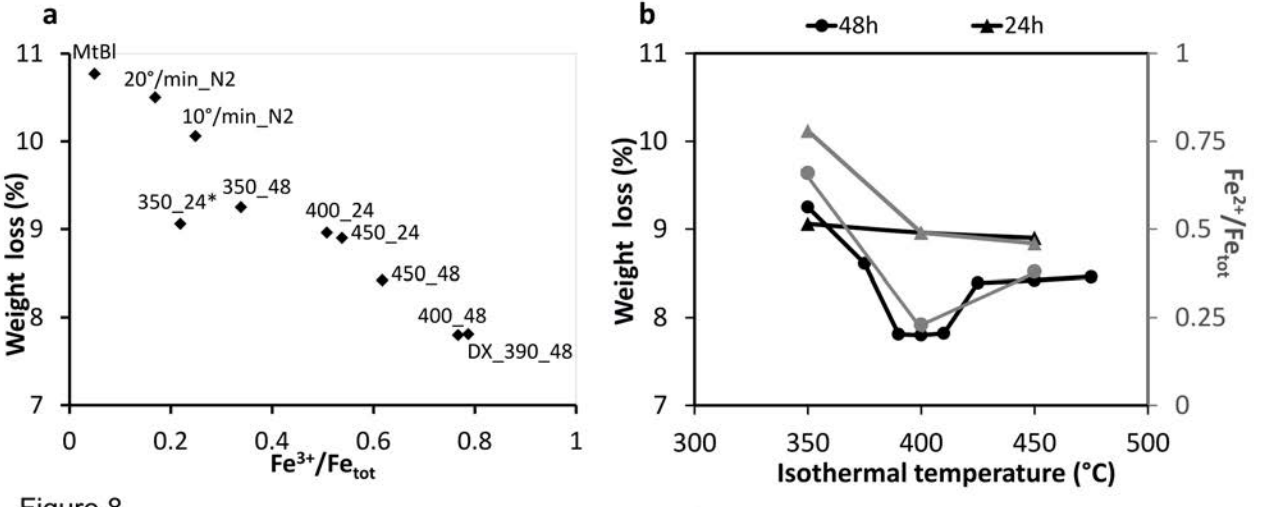

Figure 8